明志科技大學
MING CHI UNIVERSITY OF TECHNOLOGY

Master's Program of the Department of Electronic Engineering

Master Thesis

Efficient and transparent organic photodetectors with a low dark current density and high thermal stability

Graduate Student: Marvin Yonathan Hadiyanto

Advisor: Shun-Wei Liu, Ph.D

January 2022

Ming Chi University of Technology
Recommendation Letter from the Thesis Advisor

This thesis is by <u>Marvin Yonathan Hadiyanto</u> of the <u>Department of Electronic Engineering</u>, entitled: <u>Efficient and transparent organic photodetectors with a low dark current density and high thermal stability</u>, which is written under my supervision and I agree to propose it for examination.

Advisor _Shun - Wei Liu_ (Signature)

November 24th / 2021 (mm/dd/yyyy)

Ming Chi University of Technology
Thesis/Dissertation Oral Defense Committee Certification

This thesis is by___Marvin Yonathan Hadiyanto___ of the ___Master's___

Program of the Department of Electronic Engineering___,

entitled: ___Efficient and Transparent Organic Photodetectors with a Low

Dark Current Density and High Thermal Stability___, who is qualified for

master/doctorate degree through the verification of the committee.

Convener of the degree examination committee _Chih-Hao Chang_(Signature)

Committee members___Shun-Wei Liu_____Sajal Biring_

___Chih-Hao Chang_____

_____

_____

Department Chair _Ja-Fen Wu_

January / _6th_ / _2022___ (mm/dd/yyyy)

Abstract

A rapid progress in research and development of transparent organic optoelectronic devices has been recognized in recent years. However, only a small number of attempts have been addressed to the reinforcement of thermal stability. In this study, a comparison of different type of hole blocking layer (HBL), optimization of HBL thickness, thermal shock examination, and working voltage adjustment are evaluated to determine the optimum configuration for transparent photodiodes (TPDs) with high thermal stability. The optimized TPD with -0.5 V applied bias exhibit dark current density of 1.56×10^{-10} A cm^{-2}, external quantum efficiency (EQE) of 29.86%, responsivity of 0.18 A W^{-1}, specific detectivity of 2.48×10^{13} Jones, average visible transmittance (AVT) of 71.89%, and excellent thermal stability up to one hour of 100 $^{\circ}$C thermal shock. These results demonstrate the potential of TPDs in the emergence of transparent electronics applications in light detection and ranging (LIDAR) or internet of things (IoT) technologies.

Keywords: *TPD, HBL, dark current density, specific detectivity, thermal shock, thermal stability.*

Table of Contents

List of Figures

List of Tables

1 Introduction

1.1 Overview

Organic semiconductor is suitable for a wavelength-selective absorption material due to a relatively narrow absorption spectrum, which is significantly distinct with broad absorption feature of the inorganic counterpart [1]. Inorganic semiconductor has a band-like energy level that consist of high density of states (DOS) resulting from lattice periodicity of atomic bonding. Absorbed light in the inorganic semiconductor will excite delocalized valence electrons over a broad spectrum of DOS. On the other hand, organic semiconductor comprises of discrete orbitals due to the nature of its van der Waals bonding which allow photon to be absorbed by a single molecule that resulting an excited state (exciton) with an intense and narrow spectrum. Engineering of the organic material such as chemical functionalization can shift the wavelength-selective absorption spectrum into the ultraviolet (UV) or near-infrared (NIR) region to yield a higher transmittance that can be used for transparent electronic devices. This unique advantage of organic semiconductor is highly promising for the plethora transparent electronics and its applications [2].

High NIR absorption organic semiconductor materials are naturally suited with transparent solar technologies. Remarkable progress of transparent photovoltaics (TPVs) based on wavelength-selective organic material with PCE > 1% and average visible transmission (AVT) > 75% have been made [3,4]. Current wavelength-selective TPV technologies are developed with various organic materials including polymers, small molecules, salts, and nanotubes. Small molecule NIR-wavelength-selective TPV consists of planar heterojunction of fullerene (C_{60}) as the acceptor and chloroaluminum phthalocyanine (ClAlPc) as the donor were reported with

1.7% PCE and 56% AVT [5]. Polymer-based TPV of bulk heterojunction of phenyl-C61-butyric acid methyl ester (PCBM) and poly(2,60-4,8-bis(5-ethylhexylthienyl)benzo-[1,2-b;3,4-b] dithiophene-alt-5-dibutyloctyl-3,6-bis(5-bromothiophen-2-yl) pyrrolo[3,4-c]pyrrole-1,4-dione) (PBDTT-DPP) TPV with 4% PCE and 64% AVT were demonstrated [6]. Combination of small molecule acceptors and polymer donors-based TPV were proposed with PCE of 9.8% despite the low AVT of 32% [7]. Recently, highly transparent photovoltaics with the use of bulk heterojunction of $ClAlPc:C_{60}$ and transparent electrode of $Cu:Ag/WO_3$ were achieved a PCE of 1.3% and AVT of 77% [4]. The list of TPVs that have been mentioned are developed to harness the NIR light as indicate by their high NIR external quantum efficiency (EQE). The fact that most of TPV harness NIR light is due to the potential of 73.5% photon flux in the NIR region which is influential for the future development of TPV technologies [8].

The future opportunity of transparent electronics technology is very vast. The emerging technologies such as, touch screen, display, smart windows, artificial intelligence eye wears, invisible electronic circuit and transparent mobile terminal as illustrated in **Figure 1.1** require next generation of electronics devices other than TPVs [9–15]. Organic transparent photodetectors (TPDs), especially organic NIR TPDs are potentially bright for the next generation of IR photodetector (PD) to accommodate the future demand of transparent electronics. Aside from the prospect, only three reports published since 2015. An organic NIR TPD with AVT of 68.9%, dark current of 5.7×10^{-8} A cm^{-2}, and specific detectivity of 10^{-12} Jones [12] reported by Zhang et al.; Self-powered organic NIR TPD have been reported by Lau et al. with specific detectivity of 4×10^{12} Jones, dark current in the order of 10^{-8} A cm^{-2}, and AVT of 57.6% [16]. Furthermore, the latest TPDs is reported by Hadiyanto et al., their devices are based on $ClAlPc:C_{60}$ bulk-heterojunction and $Cu:Ag/WO_3$ transparent electrode that shows a dark

current density as low as 0.36 nA cm^{-2}, AVT of 76.92% and detectivity of 4.12×10^{12} Jones. However, these TPDs have a low thermal stability, with thermal shock of 100 ºC for 30 minutes the dark current density raises three orders of magnitude due to low thermal stability of BPhen as blocking layer [17]. Moreover, Hadiyanto et al. studied TmPyPB-based TPDs that yield dark current density in the order of 10^{-7} A cm^{-2} with a good thermal stability.

Figure 1.1 The Sun's illustration of transparent mobile phone [9] based on LG's US patent [10].

The dilemma between low dark current density and high thermal stability prohibits the potential of TPD towards the commercial applications. Solution of the trade-off between dark current density and thermal stability is needed to enable the application of TPDs in technologies such as LIDAR or IoT. The minimum requirement is thermal stability under 60 °C to be able to applied TPDs in those technologies [18,19]. Especially for LIDAR, this technology has been implemented in the camera system of iPhone 12 Pro as shown in **Figure 1.2** [20]. Furthermore, potential application of this technology is very promising, particularly in transparent mobile phone.

Achievement in the development of thermally stable TPDs would facilitate the emergence of transparent mobile phone in the near future.

Figure 1.2 LIDAR sensor in camera system of iPhone 12 Pro [20].

Here, an optimization the device structure of TPD to maximize the trade-off between dark current density and thermal stability is studied. This work can be summarized into three parts of experiment. First, comparison of TPD performances for different hole blocking layer, including neat C_{60}, neat CN-T2T, and mixing C_{60}:CN-T2T with 1:1 ratio. Second, optimization of the TPD performances by tuning the thickness of hole blocking layer. Third, evaluation of TPD performances before and after thermal shock with different applied bias. To evaluate performance and thermal stability of TPDs, electrical and optical measurements such as dark current density, external quantum efficiency (EQE), responsivity, specific detectivity (D*), transient photoresponse, -3dB limited frequency bandwidth (f_{-3dB}), linear dynamic range (LDR), and ultraviolet-visible (UV-vis) spectroscopy were studied in an ambient environment. Dark current density, EQE, as well as

responsivity are measured before and after thermal shock up to 4 hours. Under -0.5 V applied bias, the optimized TPDs show dark current density of 1.56×10^{-10} A cm^{-2}, responsivity of 0.18 A W^{-1}, and detectivity of 2.48×10^{13} Jones. The performances remain stable after 1 hour of 100 ºC thermal shock with dark current density of 2.72×10^{-10} A cm^{-2}, responsivity of 0.17 A W^{-1}, and specific detectivity of 1.82×10^{13} Jones after exposure.

1.2 Objective

In order to achieve an optimized device structure of TPD with a low dark current density and high thermal stability, the objectives are:

1. Implement a HBL to reduce dark current density and maintain other performance such as EQE, responsivity, and specific detectivity.
2. Tune the thickness of HBL to gain an optimum performance.
3. Utilize different working voltage for TPDs to exploit the best performance before and after thermal shock.

1.3 Outline

This thesis is divided into 5 sections, which can be summarized as the following:

Chapter 1   Introduction
This chapter explains an overview and motivations of the study of TPD.

Chapter 2   Literature Review
This chapter describe the principle of TPD and the previous work on TPD.

Chapter 3   Experimental Method
This chapter demonstrate a detail procedure of experimental methods, including materials preparation, fabrications, and measurements

Chapter 4   Result and Discussion

This chapter shows the data and the corresponding discussion of the proposed TPD.

Chapter 5   Conclusion

This chapter interprets and concludes the entire result of this work.

2 Literature Review

2.1 TPD Device Structure

Device structure of TPD is generally similar with the conventional organic PD, the main difference is the TPD consists of all transparent electrodes on the bottom and top side instead of opaque electrode on one side. As can be seen in **Figure 2.1**, device structure of TPD is comprised of transparent anode, electron blocking layer, photoactive layer, hole blocking layer, transparent cathode, and capping layer.
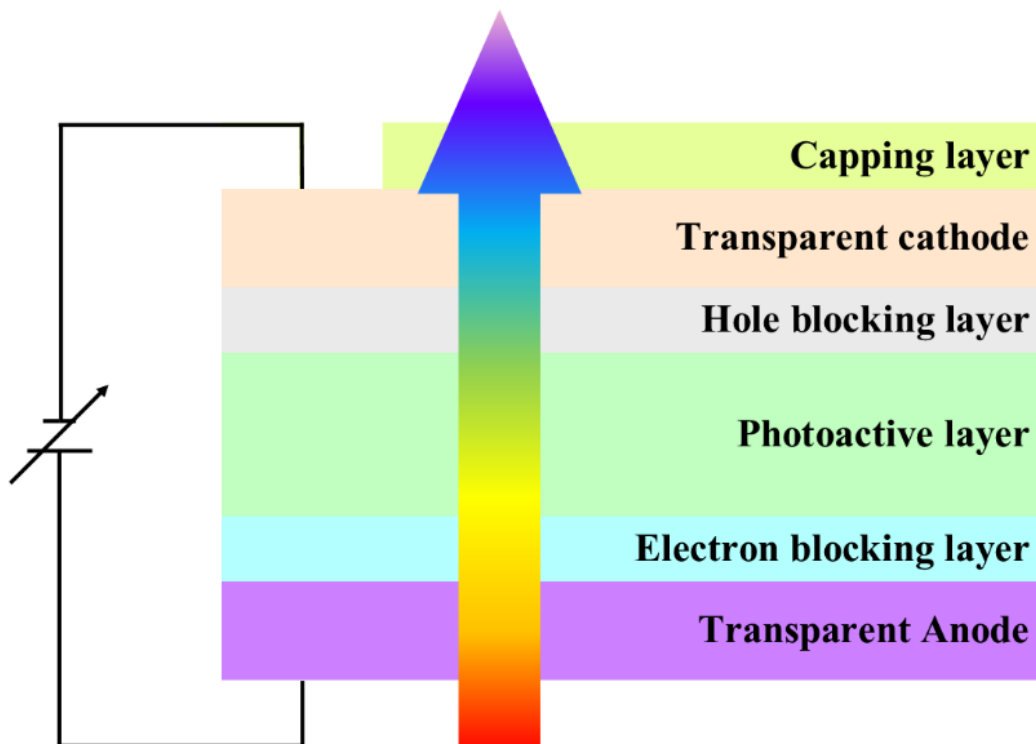
Figure 2.1 Illustration of TPD device structure.

2.1.1 Photoactive Layer

Photoactive layer absorbs and dissociates the incident light into electron-hole pair, dissociated electrons and holes diffuse to the subsequent layers and eventually extracted by the electrodes that resulting a photocurrent. Photoactive layer consists of donor (D) and acceptor (A) junction which are

typically made from D-A planar heterojunction or D-A bulk heterojunction as shown in **Figure 2.2** [21].

(a)

(b)

Figure 2.2 Illustration of (a) D-A planar heterojunction and (b) D-A bulk heterojunction in a photoactive layer.

The process of photocurrent conversion in the photoactive layer starts with photon absorption by either donor or acceptor (assume that light comes from the donor side). The photon generates exciton (step 1) that diffuses toward the D-A interface (step 2), at this interface, exciton is dissociated into electron and hole (step 3), electron is then transferred from the donor to the acceptor and hole stays in the donor (step 4) [1]. The dissociation and transfer process of exciton is driven by the driving force due to the energy offset

(ΔE_{HL}) between the donor's HOMO and the acceptor's LUMO as illustrated in **Figure 2.3**. To efficiently dissociate photon into electron and hole, parameters such as thickness, energy bandgap, and doping ratio (for bulk heterojunction) are substantial in the D-A heterojunction design.
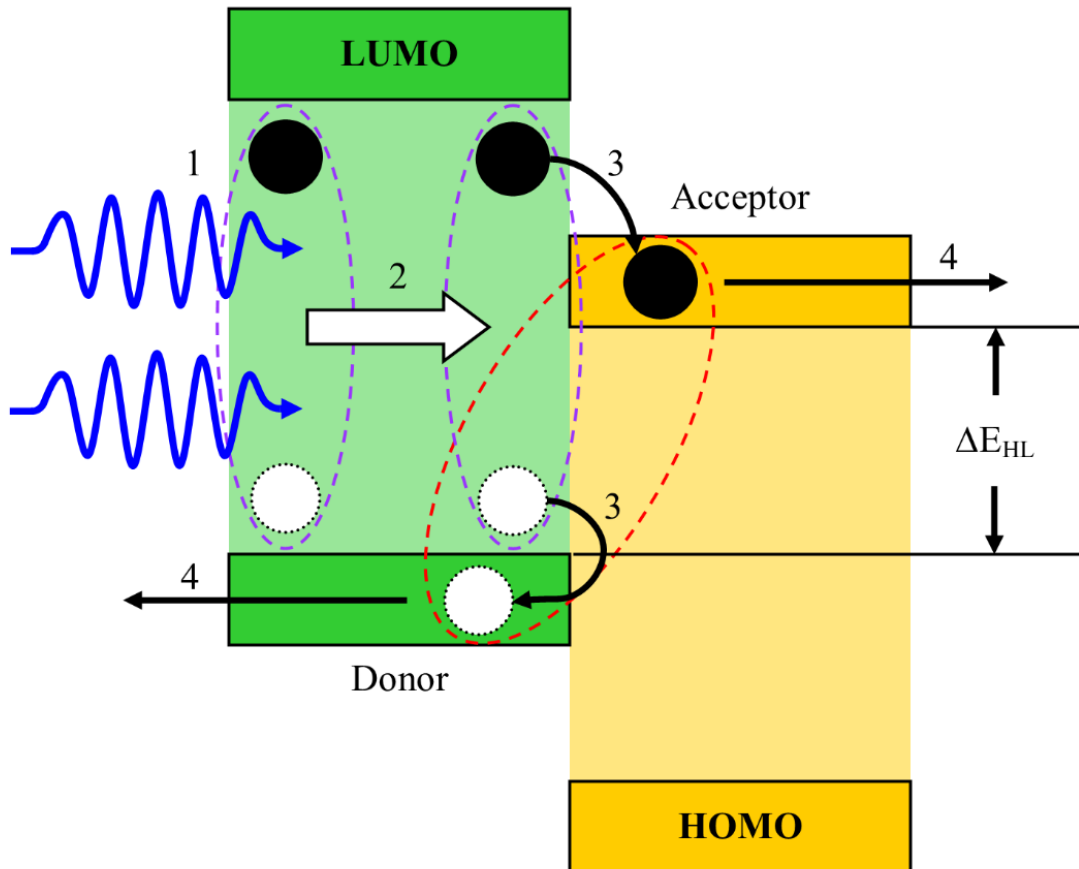
Figure 2.3 Illustration of photocurrent generation process in a D-A heterojunction. Blue sine waves indicate photons, dashed line indicate the Coulomb binding between electron and hole (purple colors indicate excitons and red color indicates dissociated exciton), black circles indicate electrons, and white circles for holes.

2.1.2 Blocking Layer

The blocking including hole blocking layer (HBL) and electron blocking layer (EBL) is a layer of wide energy bandgap material to prevent hole or electron leakage from photoactive layer to the electrodes. EBL also serves as the hole transport layer that favor hole from photoactive layer diffuse to the anode, while HBL behaves as ETL for the electron transfer as can be seen in **Figure 2.4**. Furthermore, HBL provides a protection to the photoactive

layer from damage during the metal cathode deposition and the extra thickness of device structure to ensure there is no short pathway between anode and cathode [1].
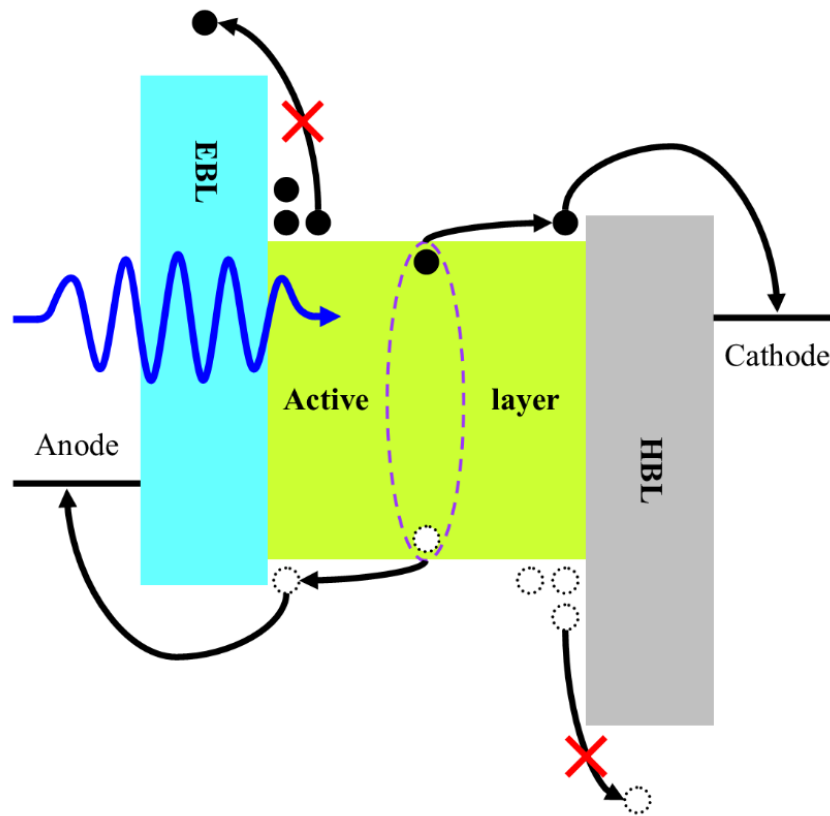
Figure 2.4 Energy level diagram of blocking layers in a device structure of TPD. In this structure, high LUMO level of EBL inhibits the electron transfer from active layer to the anode and deep HOMO level of HBL forbids the hole transfer to the cathode.

2.1.3 Transparent Electrode and Capping Layer

Transparent electrodes provide an optical window for incident light as well as an electrical contact between internal layers and external connection. Two parameters need to be considered for a transparent electrode are optical transmittance and electrical conductivity [22], indium-tin oxide (ITO) is an example of a transparent electrode with those requirements and has been widely used particularly as a transparent anode. Transparency and sheet resistance of different types of transparent electrode are shown in **Table 2.1**

Table 2.1 List of transparency and sheet resistance of different types of transparent electrode material [22,23].

Material	Transparency [%]	Sheet resistance [Ω sq^{-2}]
Indium-tin oxide	80 to 95 %	10 to 50
Thin metal layers	40 to 60 %	1 to 80
Dielectric/metal/dielectric multilayer	70 to 85 %	1 to 80
Metal alloy/dielectric	~79%	~10
Metal grids	~80 %	6 to 50
Graphene	60 to 97 %	30 to 3000
Carbon nanotube	50 to 95 %	20 to 1000
Ag nanowire	70 to 90 %	5 to 200

Despite of the superiority in the transparency and sheet resistance, ITO is one of the most stable materials in comparison with the others. However, ITO has difficulties to be deposited on top of organic materials, due to its high temperature deposition process. Alternative solutions for transparent electrodes such as thin metal layers, dielectric/metal/dielectric (DMD), and metal alloy/dielectric provide a well trade-off between process complexity and optoelectronic performances.

Capping layer is an additional thin layer on the outer side of device structure (see **Figure 2.1**). The main purpose of capping layer is to alter the optical properties of the device structure; it is electrically unconnected to the internal layers. In designing a capping layer, parameters such as refractive index or transmittance are needed to optimize the AVT.

2.2 Characterization of TPD

TPD is characterized with various measurements to study its electrical, optical, opto-electronics, and electronics properties of the device. The typical

metrics to describe TPD performance are dark current density, EQE, responsivity, specific detectivity, and AVT. However, a detailed characterization of TPD is essential to understand the underlying mechanisms and device limitations for further improvement. The characterizations which are studied in this report including, dark current density, EQE, responsivity, specific detectivity, photocurrent density (J-V), transmittance, $f_{-3 dB}$, photoresponse, LDR, and thermal shock.
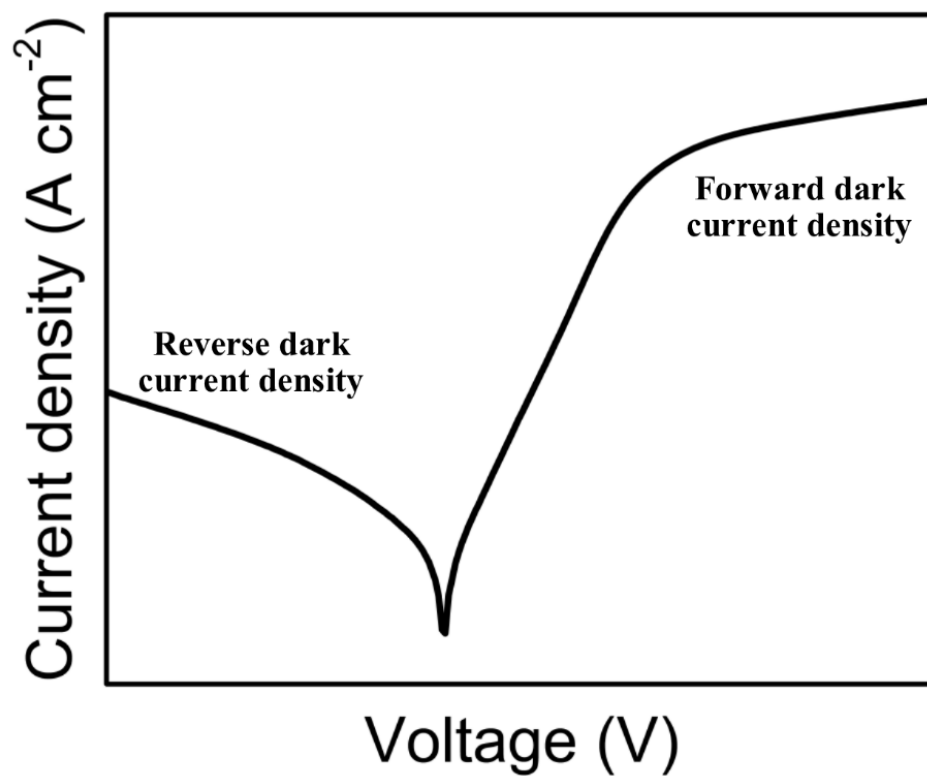
Figure 2.5 The illustration of typical J_{dark} curve. Reverse dark current density is J_{dark} in negative applied voltage bias and forward dark current density is J_{dark} in positive applied bias.

2.2.1 Dark Current Density

Dark current density is a J-V measurement under dark condition, typically it is written J_{dark}-V or simply J_{dark}. The source of J_{dark} in a TPD is mainly due to thermal generation [24,25] and charge injection from electrodes to the organic semiconductor [26–28]. In practical application,

suppressing J_{dark} is essential to gain a high photo-detection sensitivity. Strategies such as utilization of blocking layers [29], tuning the photoactive layer thickness [30], and modifying surface morphology of metal-semiconductor interface [17] have been studied to reduce J_{dark}. The illustration of J_{dark} curve is shown in **Figure 2.5**.
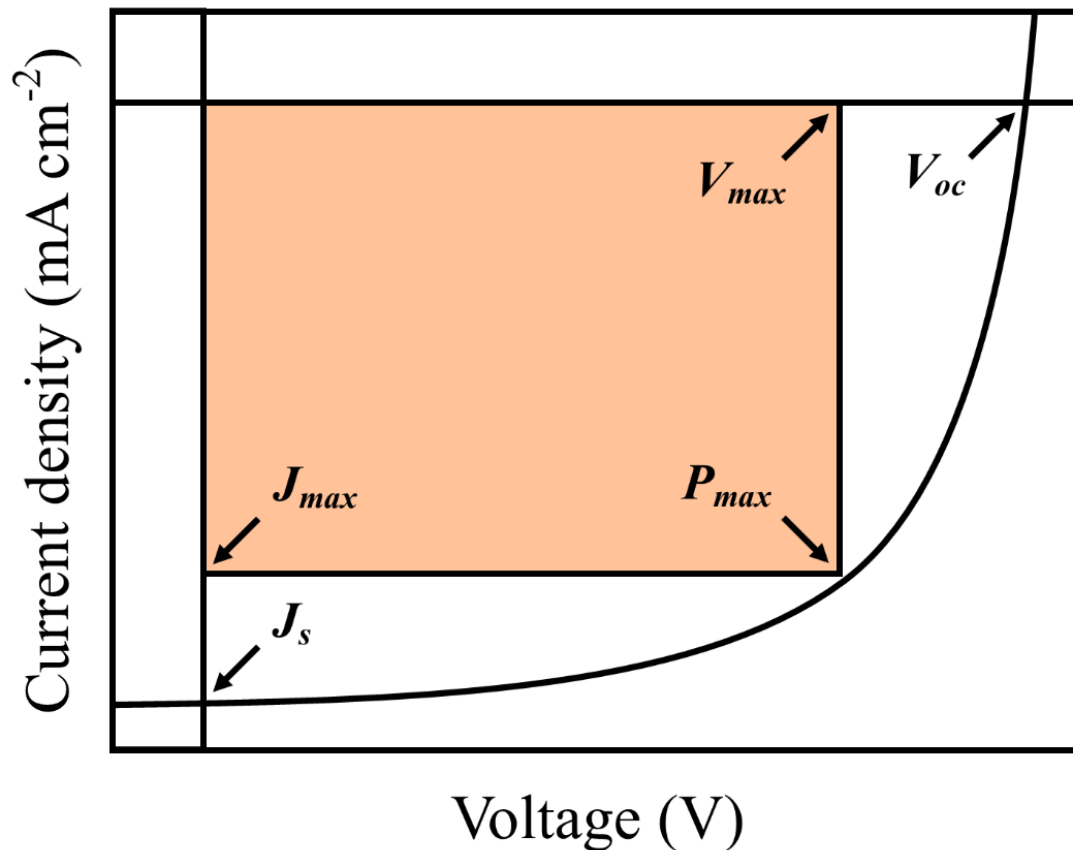
Figure 2.6 The typical J-V curve in photocurrent density measurement under one sun illumination.

2.2.2 Photocurrent Density

Photocurrent density is characterized by sweeping the applied voltage and measuring the current density while irradiating the photovoltaic with the solar spectrum AM 1.5G. From the photocurrent density curve as shown in **Figure 2.6**, parameters such as open circuit voltage (V_{oc}), short circuit current (J_{sc}), field factor (FF), and PCE (η) can be determined. V_{oc} is the voltage when current density is zero and J_{sc} is the current density when voltage is zero. Field factor is determined by the ratio of the maximum area
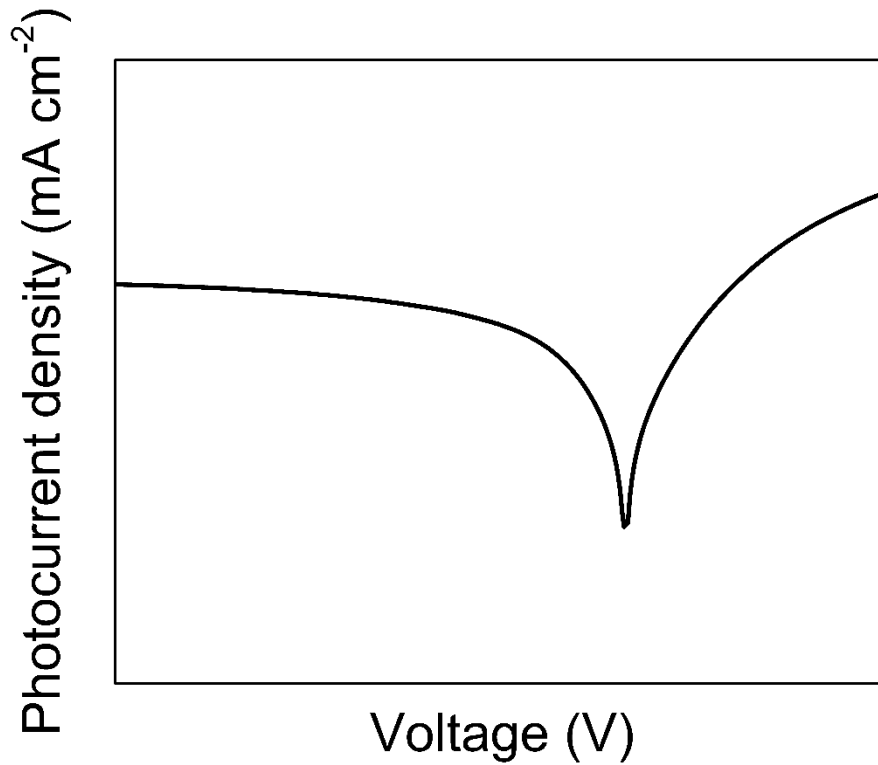
Figure 2.7 The typical plot of logarithmic scale of photocurrent density vs. voltage

(or equivalently power) in the fourth quadrant of J-V curve with respect to the $V_{oc} \times J_{sc}$. Moreover, PCE is determined by the ratio of the output power of photovoltaic respect to the input power onto it, PCE can be written by the following:

$$\eta = \frac{P_{out}}{P_{in}} \ x \ 100\% \tag{1}$$

Photocurrent density provide another approach to determining PCE of OPV, in terms of V_{oc}, J_{sc}, and FF, the PCE can be calculated by the following equation:

$$\eta = \frac{V_{oc} \ x \ J_{sc} \ x \ FF}{P_{in}} \ x \ 100\% \tag{2}$$

where:

η = power conversion efficiency of solar cell (%)

J_{sc} = short circuit current density (mA/cm^2)

V_{oc} = open circuit voltage (V)

P_{in} = power of light source (mW/cm^2)

P_{out} = output power density of solar cell (mW/cm^2)

While FF can be determined with the following equation:

$$FF = \frac{V_{max} \times J_{max}}{V_{oc} \times J_{sc}} \tag{3}$$

where:

J_{max} = current density when the delivered power is maximum (mA/cm^2)

V_{max} = voltage when the delivered power is maximum (V)

In PDs, OPDs, or TPDs analysis, photocurrent density is frequently plotted in the logarithmic scale as illustrated in **Figure 2.7,** with the photocurrent density is typically in the order of mA cm^{-2} in the reverse bias.
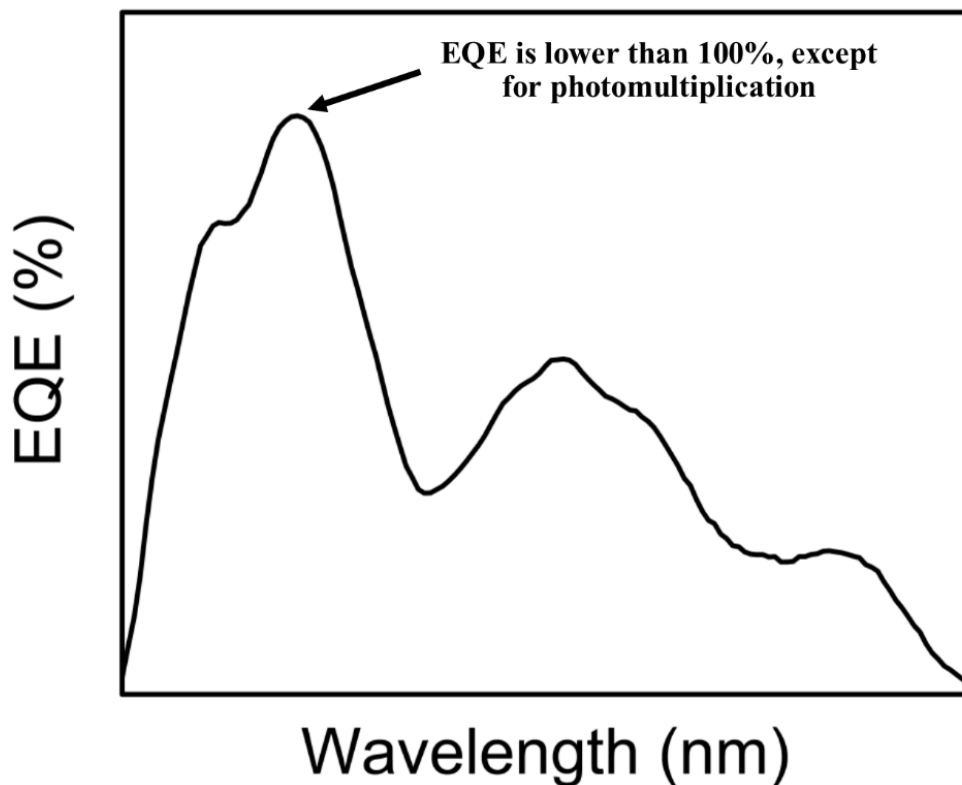
Figure 2.8 The illustration of EQE without photomultiplication effect.
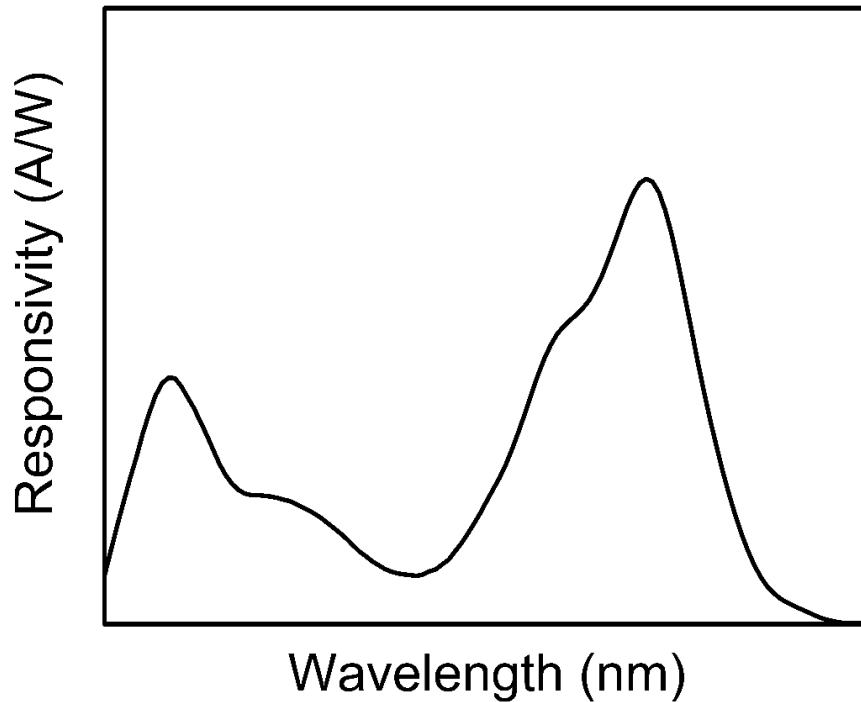
Figure 2.9 The illustration of responsivity vs. wavelength.

2.2.3 EQE and Responsivity

EQE is the ratio of the extracted electron to the incident photon irradiate onto the device. Parameters that strongly determine EQE are the absorption of donor-acceptor junction, charge transport loss from the junction to the electrode and refractive index of the device structure. The first and second parameters are determined by the intrinsic characteristics of the material, while the third parameter can be optimized by tuning thickness of the layers in the device structure. The proper design of the thicknesses will induce the optical cavity effect that can be used to enhance EQE in certain wavelength. Another method to increase EQE of organic photodetector is called photomultiplication, which can increase the EQE beyond 100%. **Figure 2.8** shows the illustration of EQE curve of TPD. Moreover, responsivity is defined as response signal of the photodetector correspond to an incident irradiation onto the photodetector, the illustration of responsivity curve can

be seen in **Figure 2.9**. Responsivity can be expressed as the following equation:

$$R = EQE \frac{\lambda q}{hc} \qquad (4)$$

where:

EQE = external quantum efficiency (%)

λ = wavelength (m)

q = electron charge (1.6×10^{-19} C)

h = Planck's constant (6.6×10^{-34} J Hz^{-1})

c = speed of light (3×10^8 m s^{-1})

2.2.4 Noise Current

Noise current is a disturbance in dark current or photocurrent that is needed to be reduced as low as possible to produce high signal-to-noise ratio. There are different types of noise current generated in TPD including, thermal noise and shot noise. Thermal noise is induced due to charge random thermal motion and this noise is inevitable [31]. Shot noise is generated from random statistical fluctuation nature of the current [32]. Shot noise and thermal noise can be expressed as the following equations:

$$I_{shot\ noise} = \sqrt{2qI_{dark}\,B} \qquad (5)$$

$$I_{thermal\ noise} = \sqrt{\frac{4kTB}{R_{sh}}} \qquad (6)$$

where:

$I_{shot\ noise}$ = shot noise (A)

$I_{thermal\ noise}$ = thermal noise (A)

q = electron charge (1.6×10^{-19} C)

I_{dark} = dark current (A)

B = normalized bandwith (1 Hz)

k = Boltzmann constant (1.38×10^{-23} J K^{-1})

T $\qquad$ = temperature (K)

R_{sh} $\qquad$ = shunt resistance (Ω)

2.2.5 Specific Detectivity

Specific detectivity (D*) is a signal-to-noise ratio value of EQE to noise of dark current [33]. D* can be calculated with the following equation:

$$D^* = R\frac{\sqrt{Af}}{i_{noise}} \tag{7}$$

where:

D^* $\quad$ = specific detecivity (Jones)

R $\quad$ = responsivity (A W^{-1})

A $\quad$ = active area of the device (cm^{-2})

f $\quad$ = normalized bandwidth (1 Hz)

i_{noise} = noise current in dark condition (A)

Specific detectivity of a TPD is expected to be a high value, the higher D* means capability to detect the weaker light signal. Moreover, the value of D* can be estimated with the noise current equivalent to the shot noise with the following equation:

$$D^* = R\frac{R}{\sqrt{2qJ_{dark}}} \tag{8}$$

Where:

D^* $\quad$ = specific detecivity (Jones)

R $\quad$ = responsivity (A W^{-1})

q $\quad$ = electron charge (1.6 $\times$ 10^{-19} C)

J_{dark} $\quad$ = dark current density (A cm^{-2})

2.2.6 Transmittance and AVT

Transmittance is the ratio of light intensity transmitted to incident light intensity. While AVT is defined as the integral of transmittance in the visible

region with the correction of human eye sensitivity, mathematically, the equation is:

$$AVT = \frac{\int_{380\,nm}^{780\,nm} T(\lambda)P(\lambda)S(\lambda)d\lambda}{\int_{380\,nm}^{780\,nm} P(\lambda)S(\lambda)\,d\lambda} \qquad (9)$$

where:

T(λ) = spectrum of transmittance

P(λ) = luminous efficacy of the human eye

S(λ) = incident light correction factor

The optical range for integration depends on the definition of visible region, in this report, optical range for AVT integration range is 380-780 nm which follows the previous work [17].
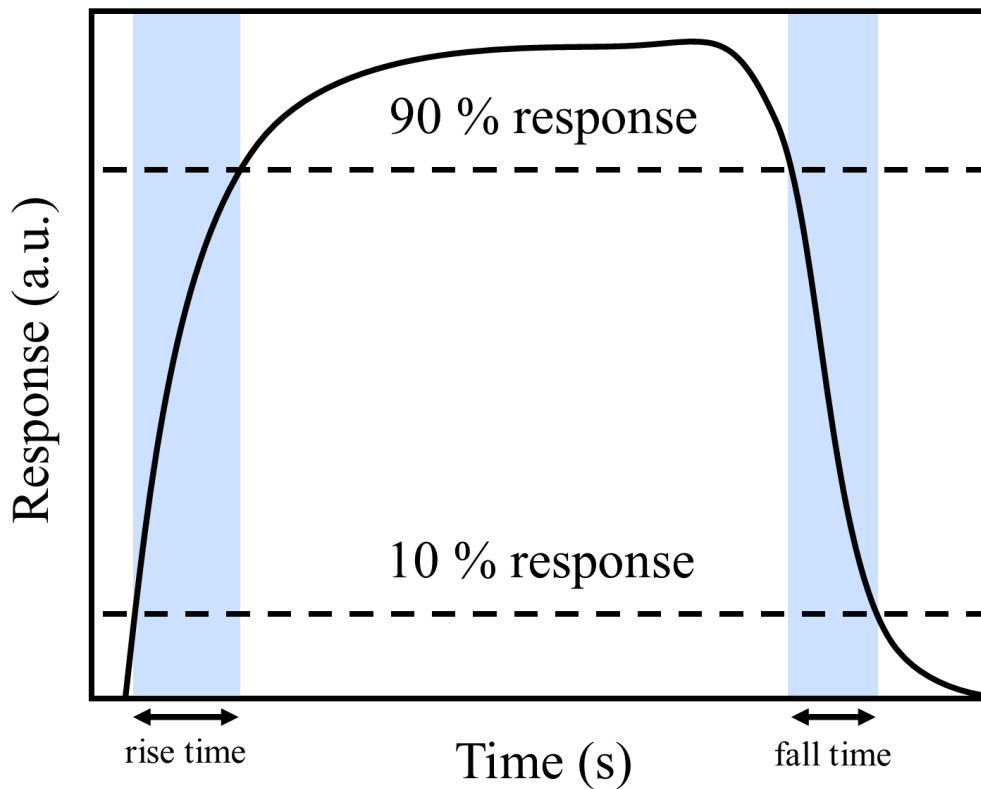
Figure 2.10 The illustration of photoresponse, rise time, and fall time.

2.2.7 Photoresponse and $f_{-3\,dB}$

Photoresponse is determined by the response signal of TPD when illuminated by a frequency-modulated or pulse of light. Parameters

19

including, cut off frequency or -3 dB signal attenuation ($f_{-3\,dB}$), rise time, and fall time are measured to determine the photoresponse characteristics of a TPD. $f_{-3\,dB}$ is determined by the carrier's transit time and RC-time constant of TPD. Typically, $f_{-3\,dB}$ is dominated by RC-time constant and mathematically written as:

$$f_{-3dB} = \frac{1}{2\pi R_t C} \tag{10}$$

where:

f_{-3dB} = cut-off frequency (Hz)

Rt   = is the total series resistance (Ω)

C   = capacitance of photodetector (F)

Rise time is defined as the amount of time that needed by the signal to rise from 10% to 90%, likewise, fall time is to fall from 90% to 10%. The illustration photoresponse can be seen in **Figure 2.10**.
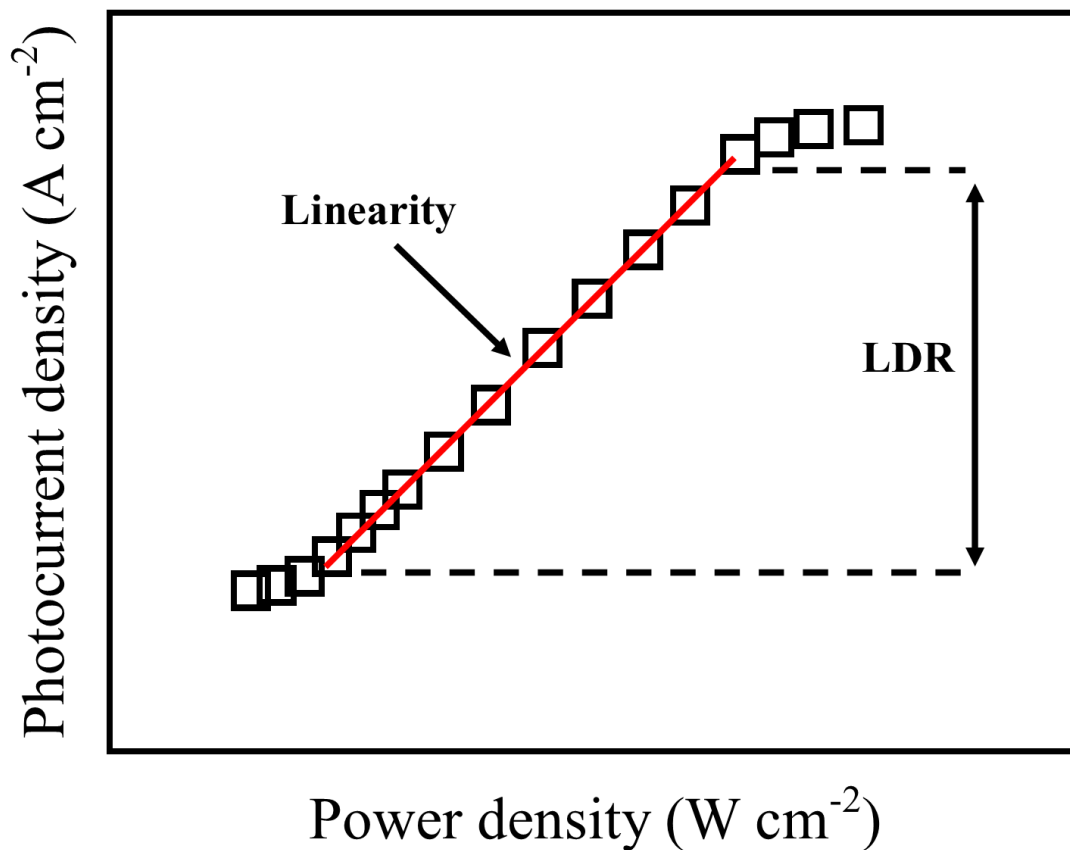
Figure 2.11 The illustration typical LDR plot.

2.2.8 LDR

LDR is the ratio of the highest to the lowest illumination intensity in which the linearity of photocurrent vs. illumination intensity hold [17,34] as can be seen in **Figure 2.11**. The LDR of OPD device is calculated with the following equation:

$$LDR = 20 \, log \left(\frac{J_{max}}{J_{min}} \right) \qquad (11)$$

where:

LDR $\quad$ = linear dynamic range (dB)

J_{max} $\quad$ = maximum photocurrent density that hold linearity (A cm^{-2})

J_{min} $\quad$ = minimum photocurrent density that hold linearity (A cm^{-2})

2.3 Previous Work in NIR TPD and Outlook
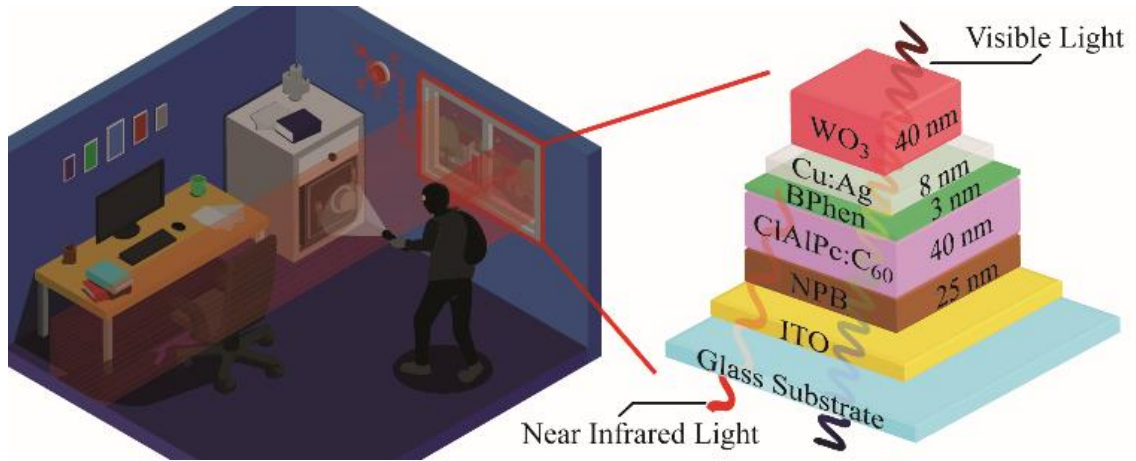
Figure 2.12 The illustration of the application and the device structure of the previous TPDs [17].

2.3.1 Previous Work in NIR TPD

Our previous work in NIR TPD implements ClAlPc:C$_{60}$ as photoactive layer and Cu:Ag/WO$_3$ as transparent electrode. The previous work proposed reference OPD with the structure of ITO/NPB (25 nm)/ClAlPc:C$_{60}$ (40 nm; 1:2)/BPhen (3 nm)/Ag (80 nm) and TPDs with the structure of ITO/NPB (25 nm)/ClAlPc:C$_{60}$ (40 nm; 1:x; with x = 2, 4, and 6)/BPhen (3 nm)/Cu:Ag (8 nm; 1:50)/WO$_3$ (40 nm) as shown in **Figure 2.12**. The optimized TPD shows

the AVT of 76.92%, dark current density of 0.36 nA cm^{-2} under -2 V applied bias, and rise/fall time < 5 µs under illumination of 780 nm light with the same applied bias. Moreover, our NIR TPD is potentially applied in a home security system by exploiting the invisible NIR detection. In comparison with other previous results in TPD or semitransparent OPD, our TPD shows the best transmittance under 515 nm and dark current density under -2 V bias voltage as can be seen in **Figure 2.13** [17].
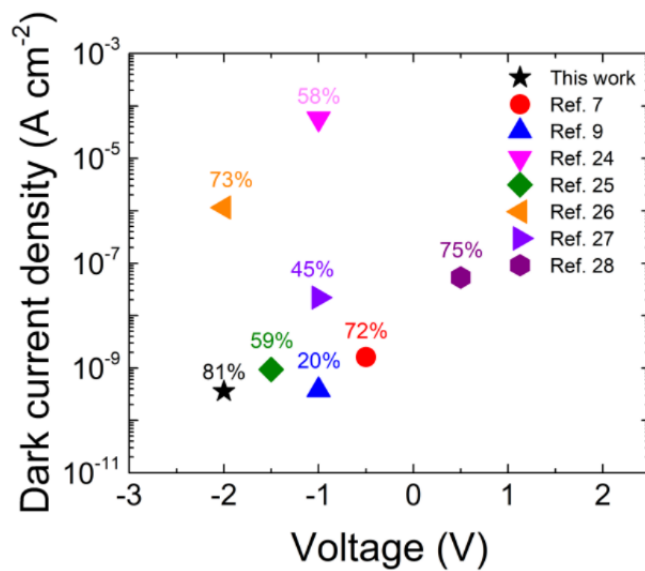
Figure 2.13 Comparison of dark current density under -2 V applied bias and transmittance at 515 nm with the other previous works on TPD and semitransparent OPD [17].

Dark current density of reference OPD and TPD with different ClAlPc:C$_{60}$ ratios in photoactive layer can be seen in **Figure 2.14**. The low dark current density of NIR TPD is attributed to the smooth surface morphology of Cu:Ag/WO$_3$ (see **Figure 2.15**). As comparison, reference OPD with the same device structure and opaque silver electrode shows a dark current density of 4.13 nA cm^{-2}. Higher dark current density of reference OPD is due to a rougher surface morphology of silver (RMS = 3.17 nm) in comparison with Cu:Ag (1.48 nm). This smoother morphology induces a less charge injection at the metal/organic interface that resulting a

lower dark current density. The performances summary of our TPDs are shown in **Table 2.2**.
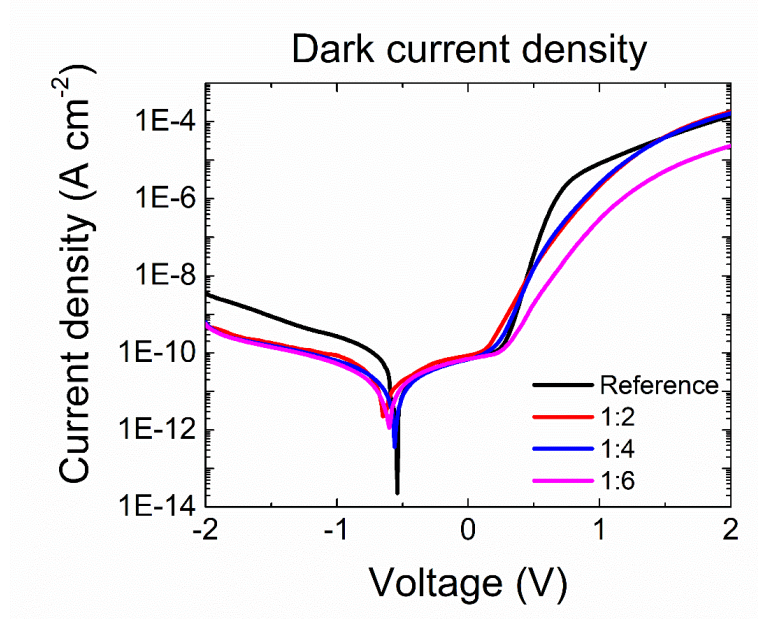
Figure 2.14 Dark current density of reference OPD and TPDs with difference ratio of ClAlPc:C_{60} in photoactive layer [17].
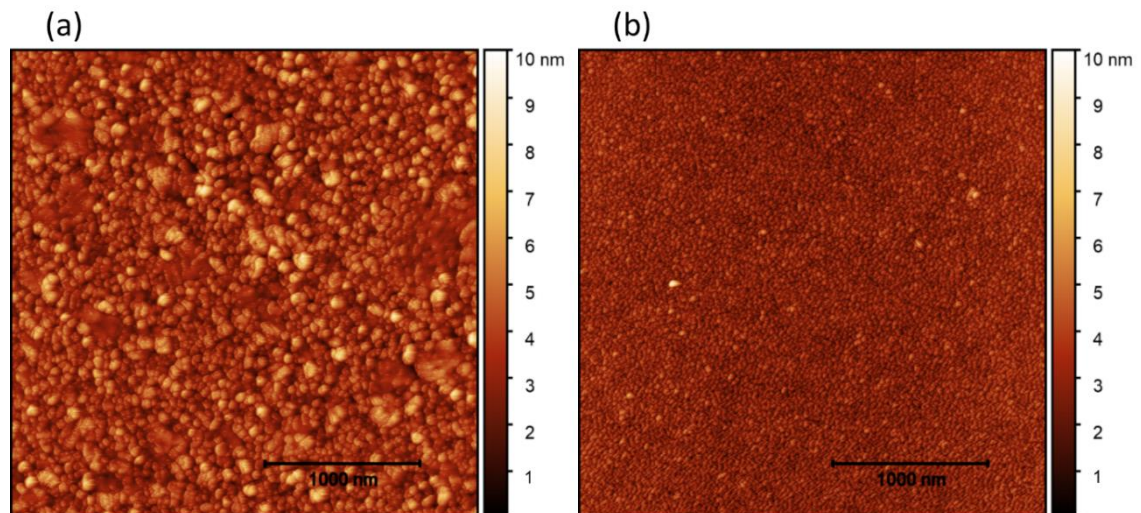
Figure 2.15 Surface morphologies by AFM for (a) 80 nm Ag (RMS: 3.17 nm) and (b) 8 nm Cu:Ag (RMS:1.48 nm) [17].

Thermal stability of our previous TPDs are examined with a thermal shock of 100 °C up to 4 hours. EQE values only slightly decrease after 4 hours of thermal shock, especially EQE in the NIR region as can be seen in

Figure 2.16. However, dark current density suffers a low thermal stability which is inherited from BPhen characteristic. Dark current density of TPDs increase by three order of magnitude after 30 minutes thermal shock of 100 °C. To substitute BPhen, alternative blocking layer material with a high thermal stability such as TmPyPb has successfully enhanced thermal stability up to 4 hours of thermal shock without any significant change in dark current density. However, dark current density of TmPyPb-based TPDs are in the order of 10^{-7} A cm^{-2} which is three order of magnitude higher than BPhen-based TPDs. Dark current density of BPhen-based and TmPyPb-based TPDs are shown in **Figure 2.17**.
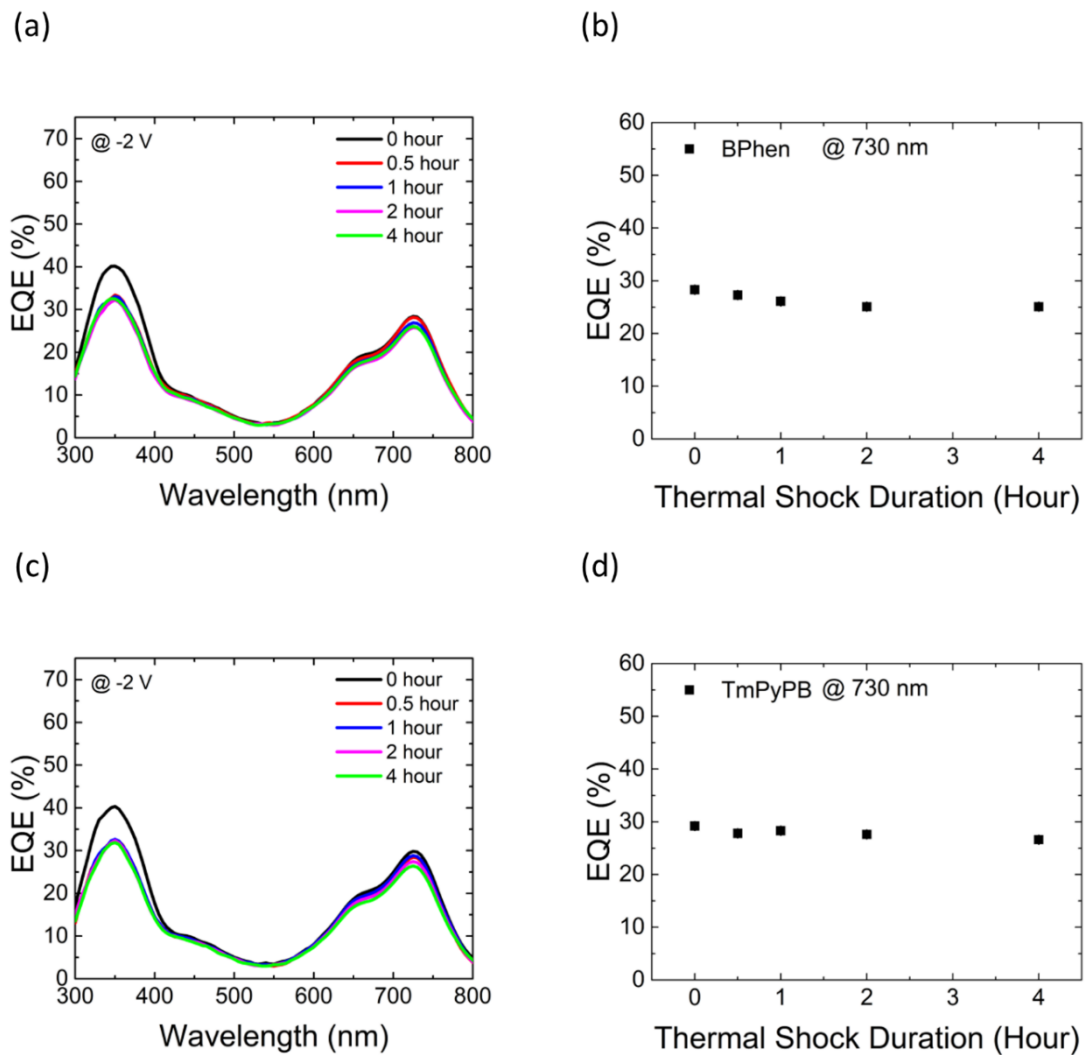
Figure 2.16 EQE of (a) BPhen-based TPDs, (c) TmPyPb-based TPDs; (b) average EQE at -2 V during thermal shock for BPhen-based TPDs and (d) TmPyPb-based TPDs [17].
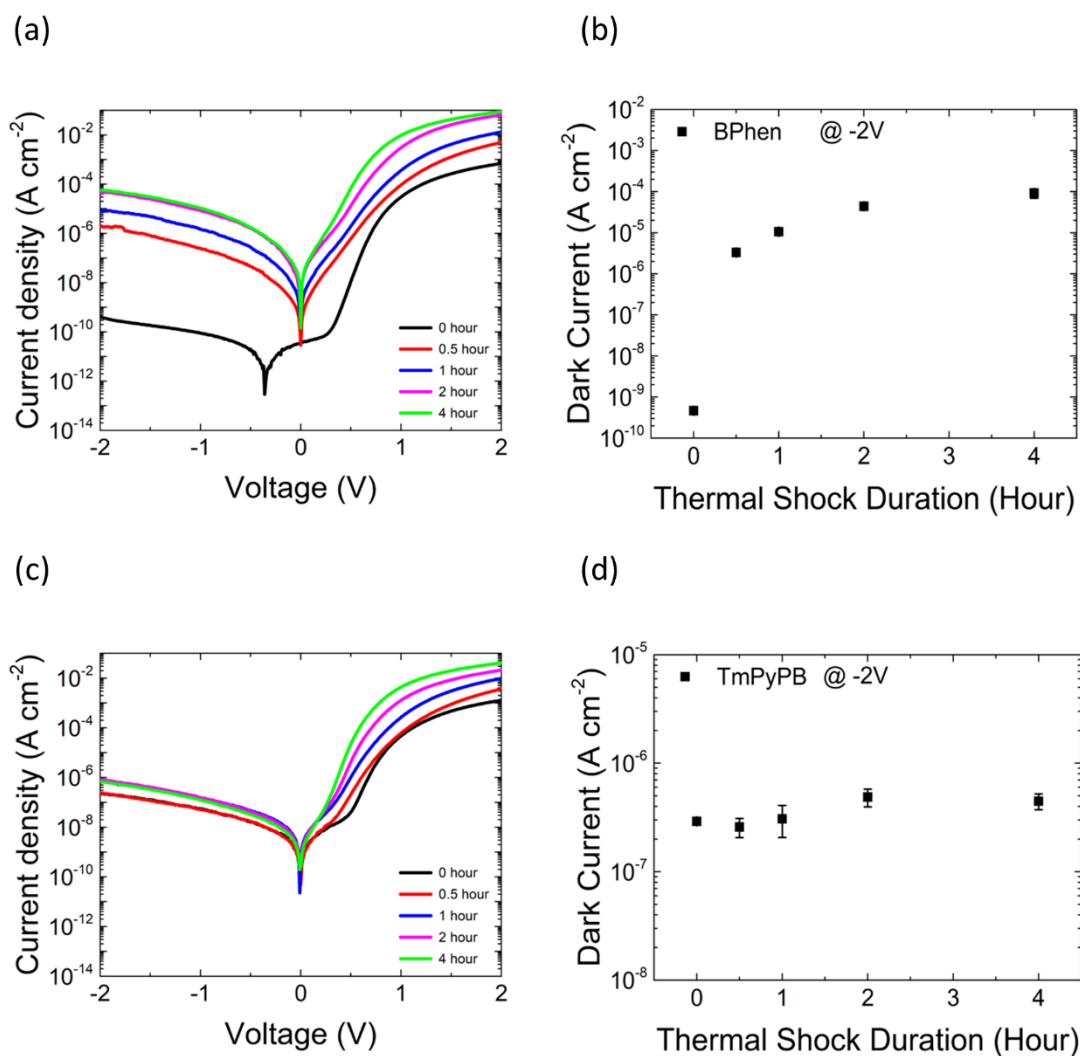
Figure 2.17 Dark current density of (a) BPhen-based TPDs, (c) TmPyPb-based TPDs; (b) average dark current density at -2 V during thermal shock for BPhen-based TPDs and (d) TmPyPb-based TPDs [17].

2.3.2 Outlook

Commercial applications such as light detection and ranging (LIDAR) or internet of things are needed the operating temperature at least 60 °C [18,19]. Conventionally, a silicon (Si) photodiode (PD) is used as the optical detector of the reflected pulse [19]. Potential of OPD or TPD utilization in LIDAR emerges owing to the rapid development of these technologies that achieve the performance nearly equivalent with Si-PD, especially for TPD, the extra feature of transparency provides a wider range of design flexibility. To realize this substitution from Si-PD to OPD or TPD, a better thermal

stability is needed. As shown in the previous work, EQE is relatively stable even after 4 hours of thermal shock at 100 °C, however, dark current density increases by three order of magnitude after 30 minutes of thermal shock at 100 °C for BPhen-based TPDs. The alternatives, TmPyPB-based TPDs offer a high thermal stability following with a high dark current density. In the future, a low dark current density and high thermal stability is needed to deliver TPD closer into LIDAR or IoT applications.

Table 2.2 Performances summary of the previous TPDs [17]

Device	J_d [nA cm^{-2}][a]	EQE [%][b]	R [A W^{-1}][c]	D* [Jones][d]	Current-gain [a.u.][e]
Ref	4.13 ± 0.36	39.4 ± 0.71	0.23 ± 0.004	1.94×10^{12}	1.77×10^6
1:2	0.36 ± 0.05	29.5 ± 0.36	0.17 ± 0.002	4.12×10^{12}	6.16×10^6
1:4	0.18 ± 0.02	28.0 ± 0.52	0.17 ± 0.003	3.22×10^{12}	6.58×10^6
1:6	0.22 ± 0.01	24.9 ± 0.54	0.15 ± 0.003	2.51×10^{11}	6.82×10^6

[a] The values are measured under -2 V applied bias; [b,c] The value of the spectral response were measured under -2 V and wavelength 730 nm; [d] The values are calculated from **eq. (7)**, where A = 0.04 cm^2 and normalized bandwidth f = 1 Hz. [e] The current-gain was calculated by J_{photo}/J_{dark} under -2 V.

3 Experimental Methodology

3.1 Materials and Device Fabrication

3.1.1 Materials

All organic and inorganic materials were obtained from Merck KGaA (Sigma-Aldrich) i.e., 1,1-Bis[(di-4-tolylamino)phenyl]cyclohexane (TAPC), molybdenum oxide (MoO_3), chloroaluminum phthalocyanine (ClAlPc), fullerene (C_{60}), 3′,3‴,3‴‴‴-(1,3,5-triazine-2,4,6-triyl)tris(([1,1′-biphenyl]-3-carbonitrile)) (CN-T2T), copper (Cu), silver (Ag), and tungsten trioxide (WO_3). Only ClAlPc had been sublimated two times by a homemade purification system under a vacuum level of $\approx 2 \times 10^{-5}$ torr prior to the fabrication process.
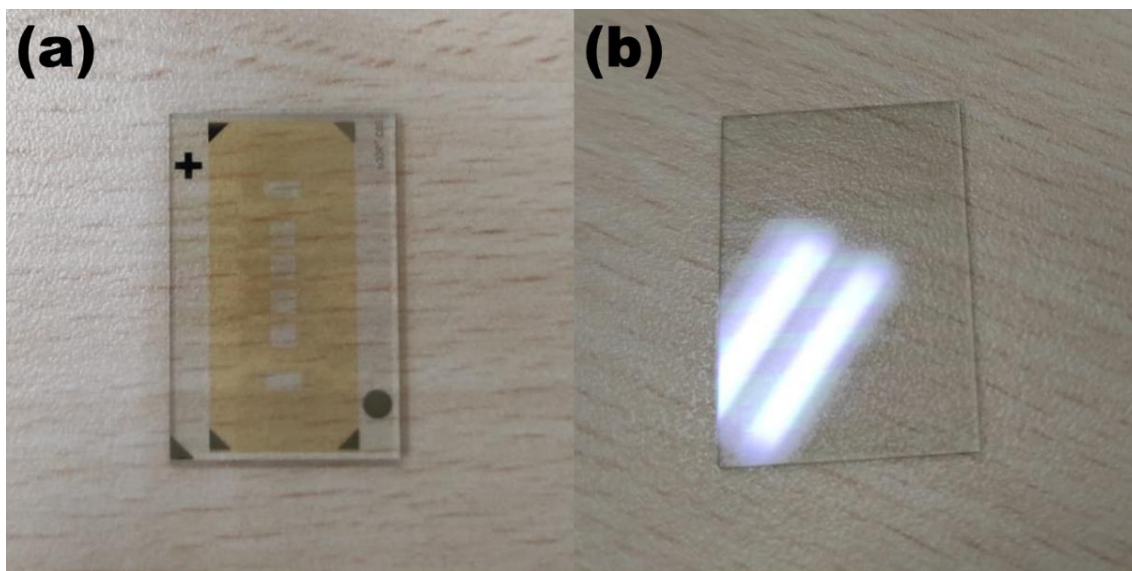
Figure 3.1 Substrates for fabrication process, (a) RitDisplay ITO and (b) laser patterned ITO.

3.1.2 Substrate Preparation

Substrate for deposition process is comprised of glass and indium tin oxides (ITO). There are two type of substrates that used in fabrication process as can be seen in **Figure 3.1**, including patterned ITO-coated glass

substrate (29×19 mm^2; 4 pixels; RiTdisplay Corporation) and ITO-coated ($15\ \Omega$ sq^{-1}; Lumtec). ITO-coated from Lumtec had been laser patterned (28×18 mm^2; 5 pixels) before the deposition process. Substrates are cleaned by the following steps (see **Figure 3.2**):
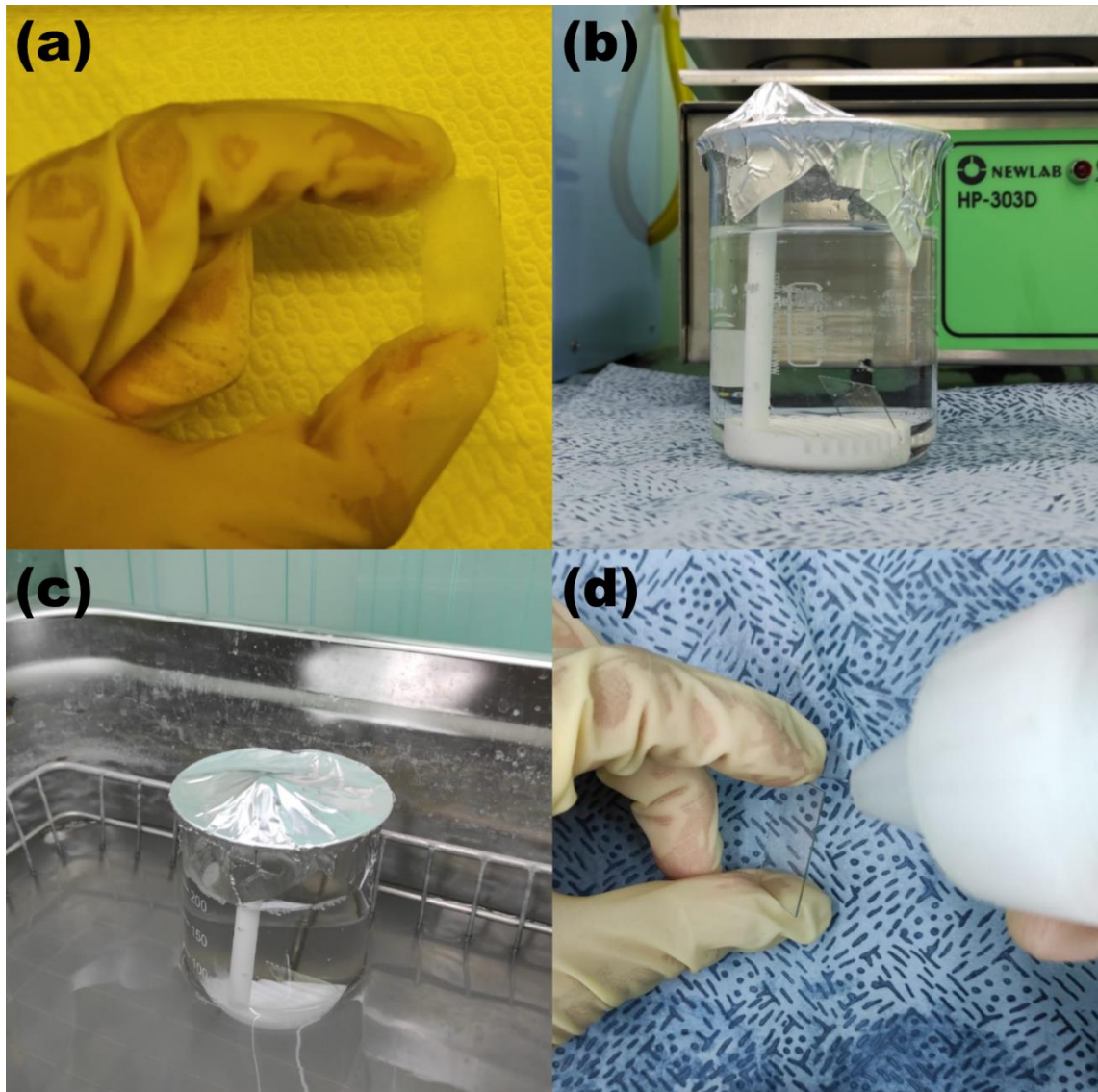
Figure 3.2 Steps of substrate preparation processes. (a) the substrate is rinsed by the soap, (b) the substrate is soaked in the liquid, and (c) vibrated with the ultrasonic cleaner for ten minutes. (b) and (c) are repeated for two times with deionized water, aceton, and isopropyl alcohol, then the substrate is dried with N$_2$ gas.

1) Substrates are rinsed by the soap, soaked in the deionized ultrasonic, and vibrated by the ultrasonic vibration for ten minutes. Substrates are soaked and vibrated two times.

2) Deionized water is changed by the acetone then vibrated by the ultrasonic vibration for ten minutes.

3) Acetone is changed by the isopropyl then vibrated by the ultrasonic vibration for ten minutes.

4) Substrates are dried by nitrogen gas.

Table 3.1 Deposition layer of device structure with different HBL.

	Organic Mask			Cathode Mask	Organic mask
RiTdisplay ITO	TAPC : MoO$_3$ 0.5 Å/s : 0.05 Å/s 25 nm	ClAlPc : C$_{60}$ 0.1 Å/s : 0.2 Å/s 40 nm	C$_{60}$ 0.2 Å/s 10 nm	Cu : Ag 0.05 Å/s : 2.5 Å/s 8 nm	WO$_3$ 0.3 Å/s 30 nm
			CN-T2T 0.2 Å/s 10 nm		
			CN-T2T : C$_{60}$ 0.2 Å/s : 0.2 Å/s 10 nm		

Table 3.2 Deposition layer of device structure with different thickness of CN-T2T.

	Organic Mask			Cathode Mask	Organic mask
RiTdisplay ITO	TAPC : MoO$_3$ 0.5 Å/s : 0.05 Å/s 25 nm	ClAlPc : C$_{60}$ 0.1 Å/s : 0.2 Å/s 40 nm	CN-T2T 0.2 Å/s 10 nm	Cu : Ag 0.05 Å/s : 2.5 Å/s 8 nm	WO$_3$ 0.3 Å/s 30 nm
			CN-T2T 0.2 Å/s 20 nm		
			CN-T2T 0.2 Å/s 30 nm		
			CN-T2T 0.2 Å/s 40 nm		

3.1.3 Device Fabrication

Device is fabricated by thermal evaporation method inside the vacuum chamber with vacuum level of 10^{-6} torr or below. Organic materials are deposited sequentially with certain masking as can be seen in **Figure 3.3**. Device structures which are deposited in this report are shown in **Table 3.1**

and **Table 3.2**. The first part of device structure is proposed to compare the performance of TPD with different HBL of C_{60}, CN-T2T, and C_{60}:CN-T2T, while the second part is the optimization of HBL thickness.
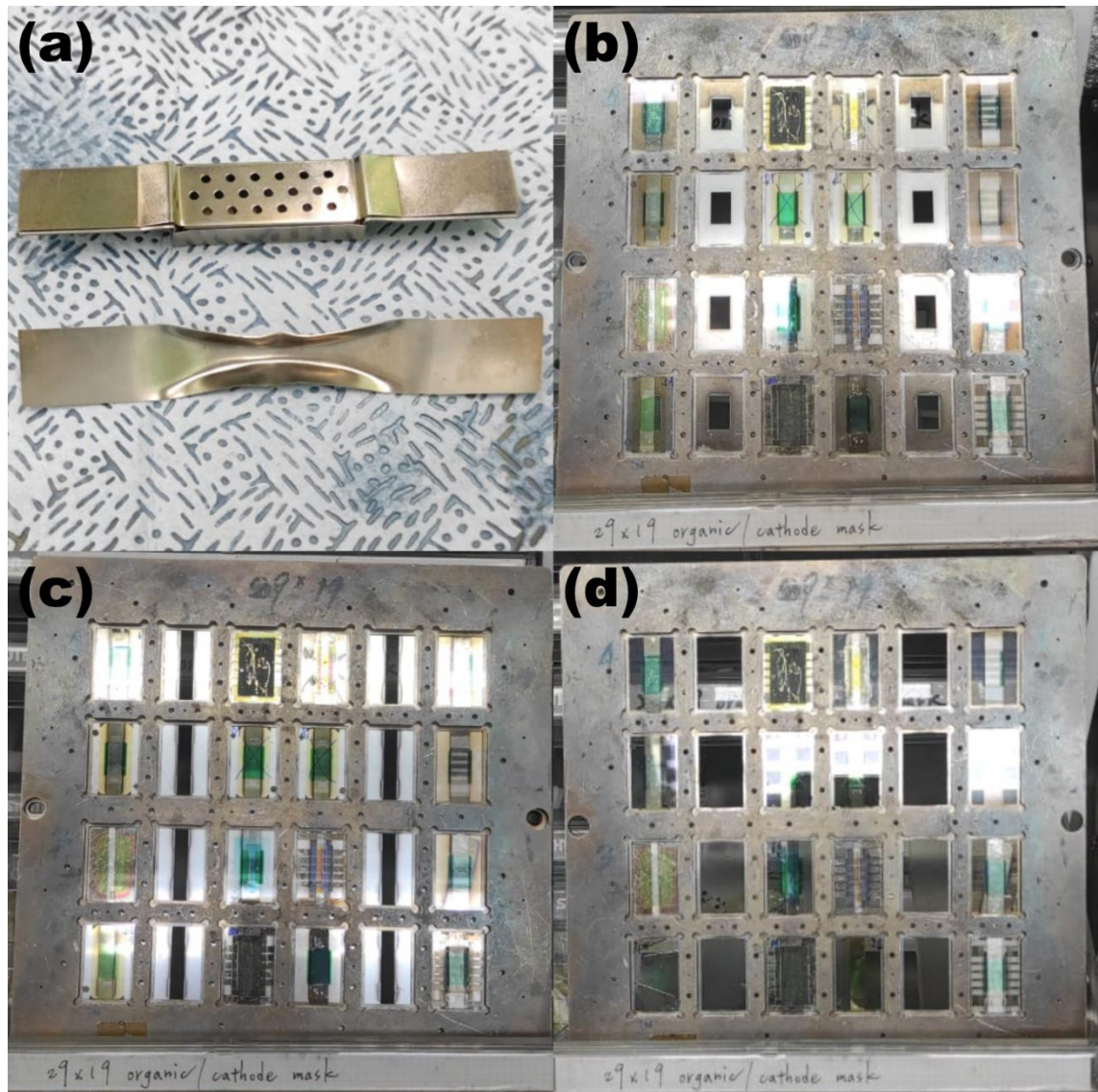
Figure 3.3 Masks and boats for vacuum thermal evaporation. (a) Hollowed-boat is organic boat and the other one is metal boat, (b) organic mask for organic layer and capping layer deposition, (c) cathode mask for cathode deposition, and (d) full size mask for thin film deposition.

3.1.4 Encapsulation

There are two type of encapsulations that used in the experiment, encapsulation glass for opaque OPD and bare glass for TPD as can be seen in **Figure 3.4**. After thermal deposition process, devices are encapsulated

(encapsulation size: 27×12 mm^2) and sealed with a UV-curable adhesive, then encapsulated devices are illuminated by UV light for 90 seconds. Bare glass and encapsulation glass are cleaned by the same procedure as substrates before the encapsulation process. Device encapsulation is processed in the nitrogen gas (N$_2$) glovebox with oxygen (O$_2$) and moisture level < 0.1 ppm.
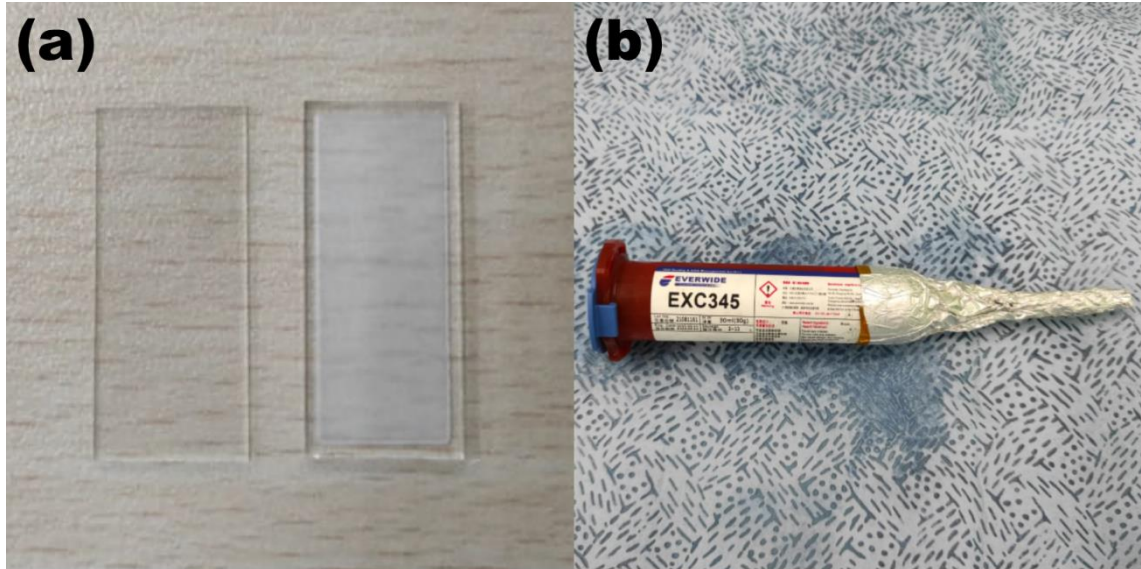
Figure 3.4 Tools for encapsulation, (a) bare glass on the left and encapsulation glass on the right, and (b) UV-curable adhesive.

3.1.5 Thin Film Preparation

Thin film is fabricated for the characterization purposes such as sheet resistance, transmittance, reflectance, absorbance, and surface morphology. Thin film is deposited on the pre-cleaned and un-patterned ITO with the same cleaning and thermal evaporation method, however thin film is not encapsulated. Thin film is kept in the N$_2$ glovebox before the measurement to prevent the degradation process due to ambient environment.

3.2 Device Characterization

3.2.1 Dark Current Density

Dark current density is measured by Keithley 2636A SYSTEM SourceMeter (see **Figure 3.5**) with the voltage swept from 2 to -2 V, 0.01 V

voltage step, and area of 0.04 cm^{-2}. The data is then collected and preprocessed into excel format by Labview software.

(a)

(b)
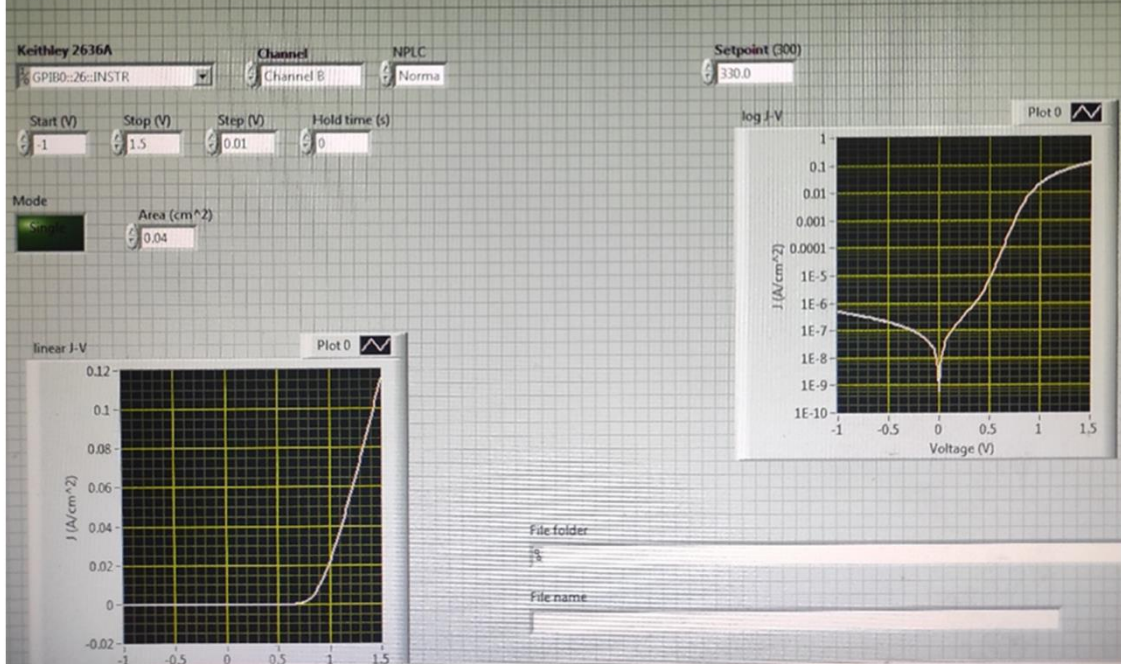
Figure 3.5 (a) Keithley 2636A SYSTEM SourceMeter and (b) Labview software of dark current measurement system.

3.2.2 Photocurrent Density

Photocurrent density is measured by one sun system which consists of solar simulator light source and keithley 2401 SourceMeter for J-V characterization (see **Figure 3.6**). Solar simulator firstly pre-heated for 30
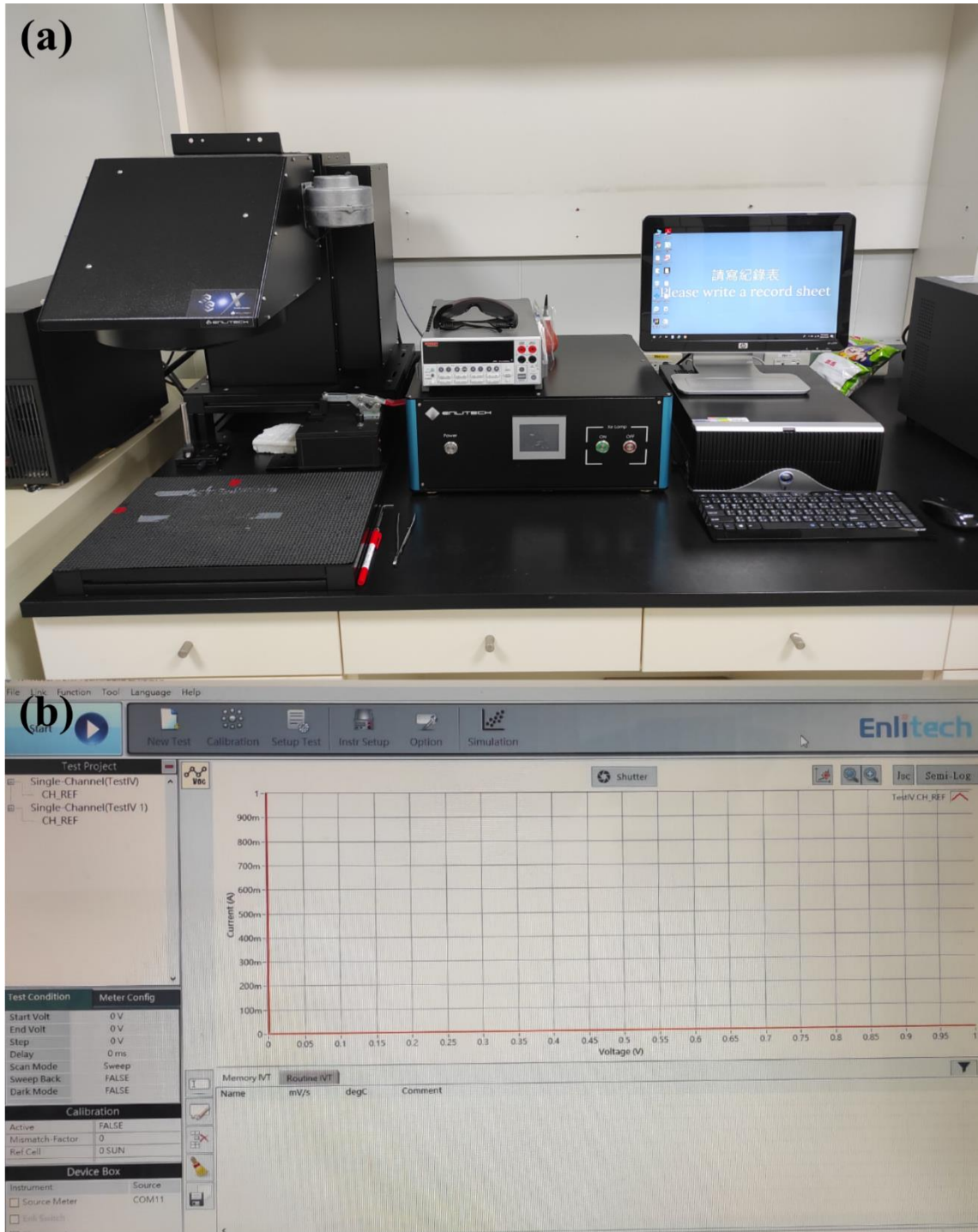
Figure 3.6 (a) One sun system and (b) Elitech software for photocurrent measurements

minutes before it is used. After pre-heated, solar simulator is calibrated with the standard silicon solar cell (1 sun illumination is equivalent of photocurrent of 75.6 mA at 0 V). The measurement is taken from -2 V to 2 V with 0.025 V voltage sweep. The result is expected to be a "J-shaped

curve" for solar cell and "S-shaped curve for photodetector". Parameters that can be extracted from one sun measurement are short circuit photocurrent (I_{sc}), open circuit photovoltage (V_{oc}), maximum solar cell power (P_{max}), efficiency, fill factor, short circuit photocurrent density (J_{sc}), series resistance (R_s), and shunt resistance (R_{sh}).

Figure 3.7 (a) QE-R system and (b) software for EQE and responsivity measurement.
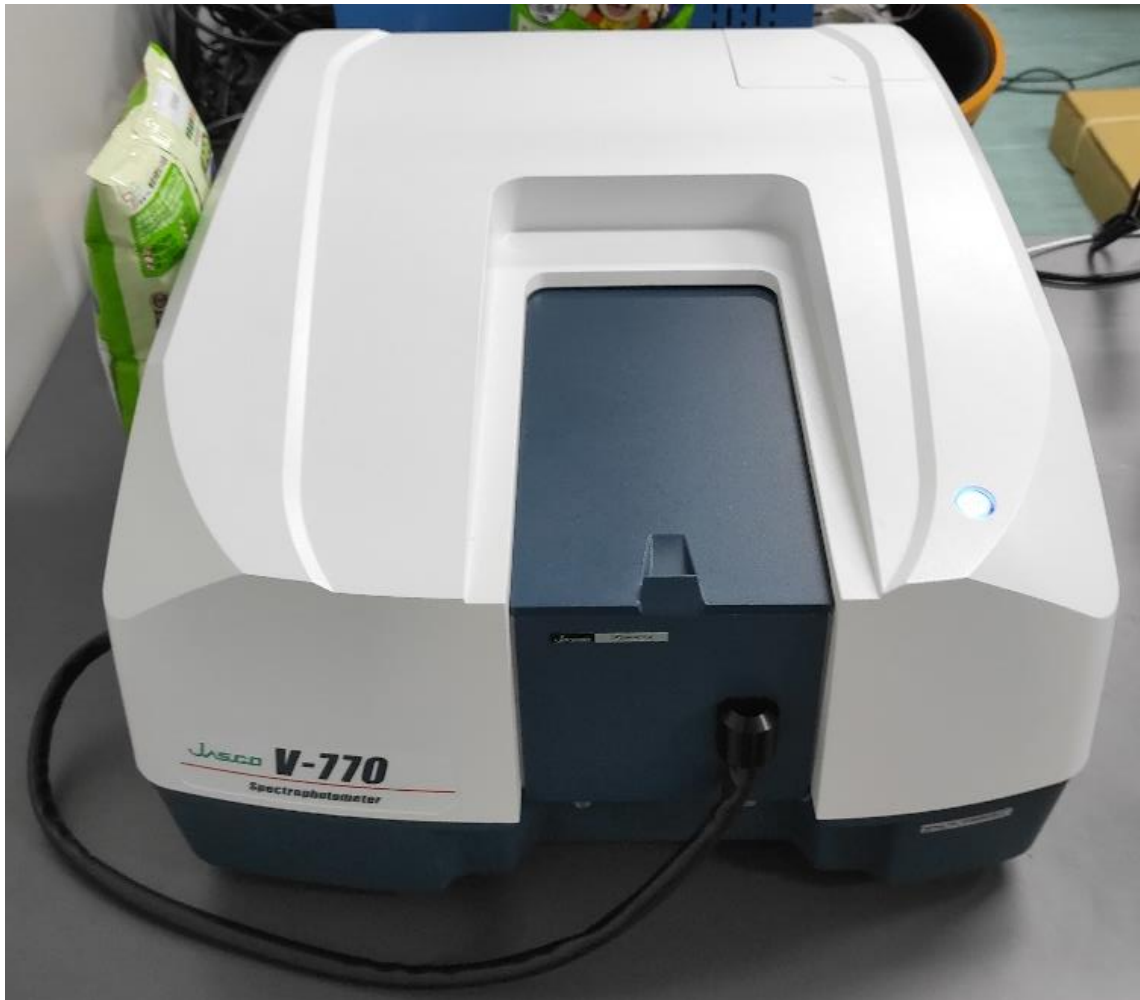
Figure 3.8 UV-vis spectrophotometer for transmittance measurements.

3.2.3 EQE and Responsivity

EQE is carried out by QE-R (Enli Technology Co., Ltd., Taiwan) as shown in **Figure 3.7**. QE-R is the system that consists of controllable wavelength light source (300-1800 nm), silicon calibrator (300-1100 nm), germanium calibrator (800-1800 nm). Before this system is being used, light source must be pre-heated for 30 minutes then calibrated by the silicon or germanium standard reference sensor; EQE is measured with AC mode. Measurement is taken under 300 to 900 nm wavelength with 5 nm step of light source under the applied bias 0, -0.5, -1, and -2 V. Responsivity data are included in the EQE data that generated by EQ-R system.

3.2.4 Transmittance and AVT

Transmittance is measured by the UV-vis spectrometer (Jasco V-770) as shown in **Figure 3.8**. Measurement is taken from the wavelength of 300-900 nm with 10 nm step. From the transmittance curve, the AVT can be calculated by using the **eq. (9)**.
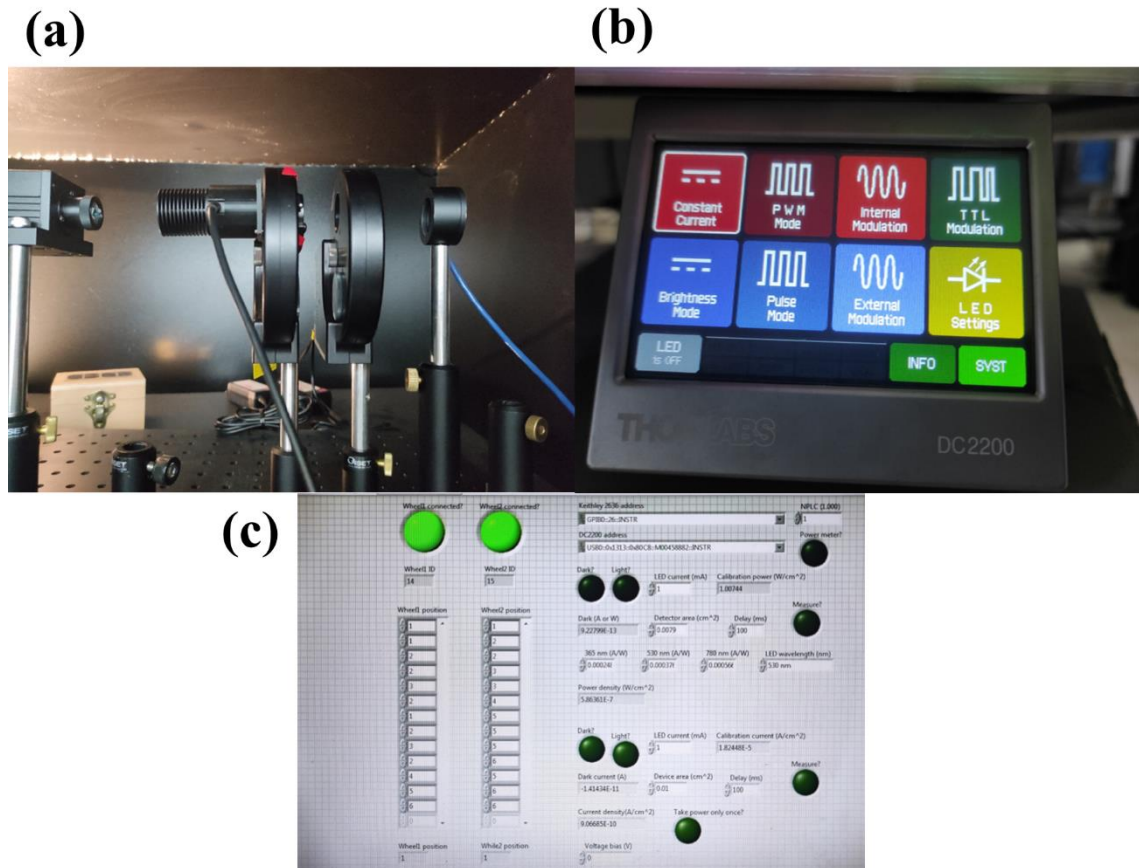
Figure 3.9 (a) Filter wheel, (b) light source system, and (c) Labview software for LDR measurement.

3.2.5 LDR

LDR is measured by the homemade set up, 780 nm light source system (Thorlabs, M780L3) is directed to filter wheel (Thorlabs, FW102CNEB) to control the light intensity as can be seen in **Figure 3.9**. Light intensity is swept from 1 mW cm^{-2} to 1 nW cm^{-2}, and the resulting photocurrent is measured by Keithley 2636A SYSTEM SourceMeter. The data are collected by Labview software and preprocessed into excel format.
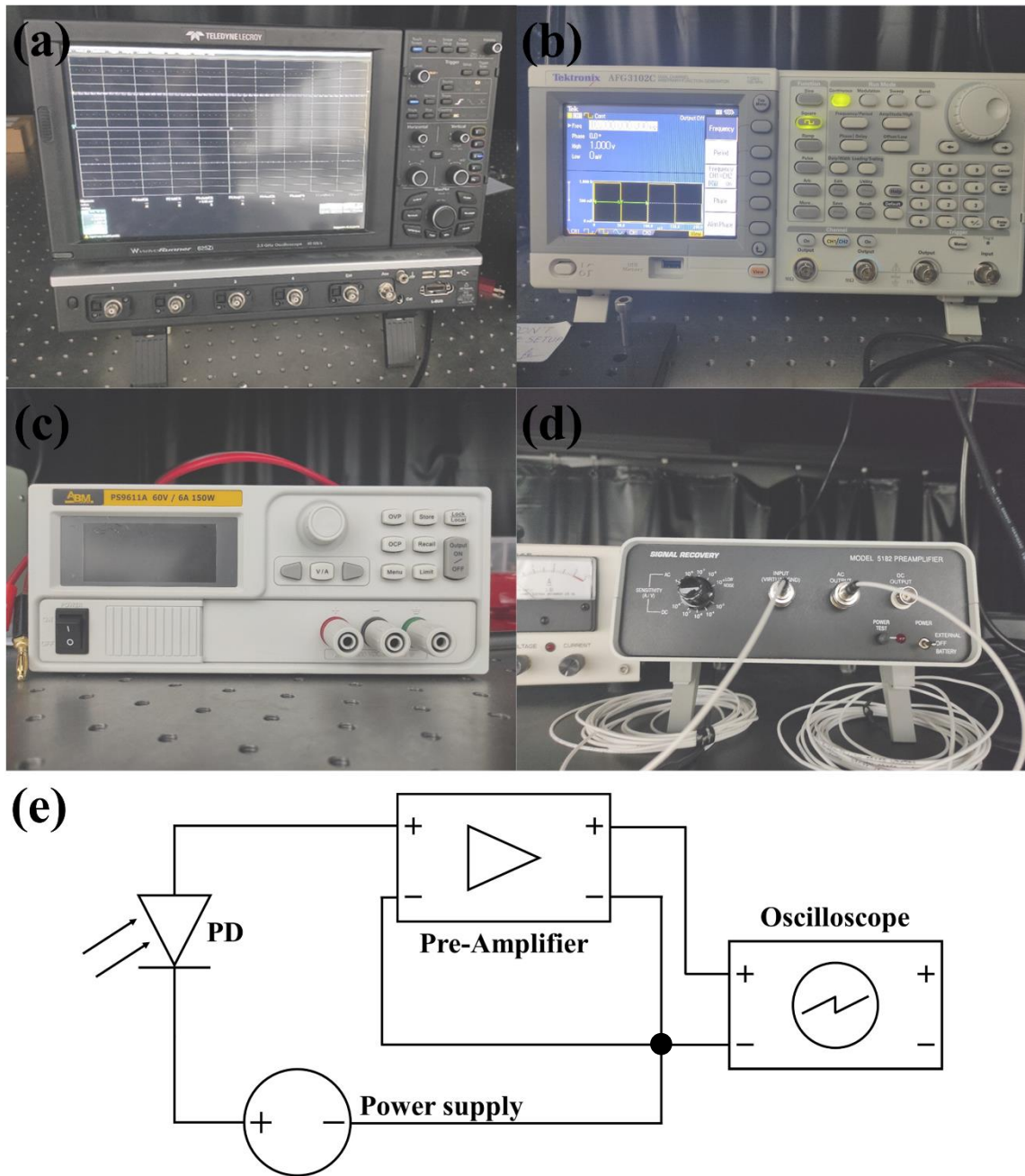
Figure 3.10 (a) Oscilloscope, (b) function generator, (c) power supply, (d) pre-amplifier, and (e) schematic of photoresponse measurement setup.

3.2.6 Transient Photoresponse

The setup for transient photoresponse measurement consists of 780 nm LED (Thorlabs) with the intensity of 1 mW cm^{-2} 10 kHz controlled by function generator (Tektronix, AFG3102C) and directed to TPD. Signal from photodetector is amplified by the pre-amplifier (Ametek, model 5182) with gain factor of 10^5 and displayed by 2.5 GHz oscilloscope (Teledyne

LeCroy, WaveRunner 625Zi). Instruments and measurement setup for transient photoresponse can be seen in **Figure 3.10**.

3.2.7 Thermal Shock

Thermal shock is carried out by the hot plate (YS-200S, Yotec) as shown in **Figure 3.11** with the temperature of 100 °C and durations for 1, 2, 3, and 4 hours. The performance of dark current density and EQE are measured before and after the thermal shock to examine the thermal stability.

Figure 3.11 Hotplate for thermal shock treatment.

4 Result and Discussion

4.1 Selection of HBL

Device structure in this work is comprising of ITO/TAPC:MoO_3 (10:1, 25 nm)/ClAlPc:C_{60} (1:2, 40 nm)/HBL (10 nm)/Cu:Ag (1:50, 8 nm)/WO_3 (30 nm). HBLs in the device structure are C_{60}, CN-T2T, and mixing C_{60}:CN-T2T with ratio 1:1. Dark current density of the device structure with different HBL is shown in **Figure 4.1**. Under -2 V applied bias, TPDs with HBL of C_{60} and C_{60}:CN-T2T show dark current density in the order of 10^{-7} A cm^{-2}, while HBL of CN-T2T shows a dark current density of 9.32×10^{-8} A cm^{-2}. The lower dark current density with HBL of CN-T2T can be attributed to the lower HOMO level of CN-T2T in comparison with C_{60} [35]. As shown in **Figure 4.2**, HOMO level of CN-T2T is 6.7 eV and C_{60} is 6.2 eV, the lower HOMO level of CN-T2T is more effective to block holes penetration from active layer into metal cathode. The values of dark current density in **Figure 4.1** at applied bias of -0.5, -1, and -2 V is shown in **Table 4.1**.
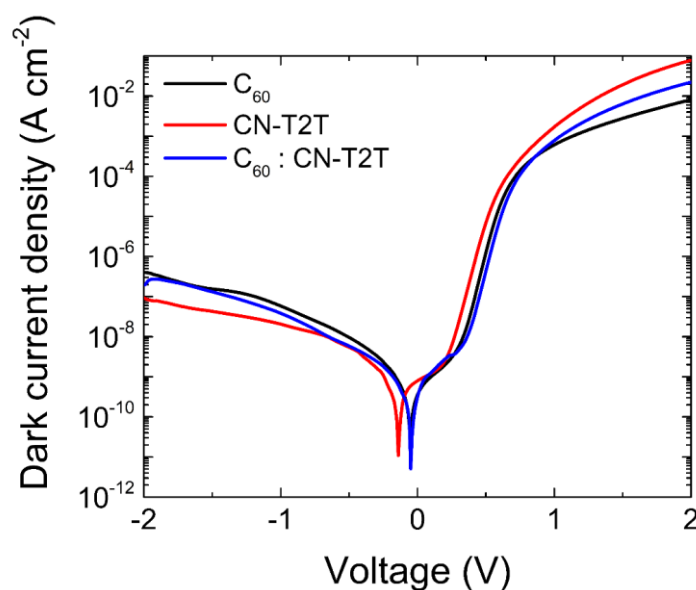
Figure 4.1 Dark current density of TPDs with HBL of C_{60}, CN-T2T, and C_{60}:CN-T2T (1:1).

Table 4.1 Summary of dark current density at different point of voltage with HBL of C_{60}, CN-T2T, and C_{60}:CN-T2T (1:1).

HBL	Dark current density		
	-0.5 V [A cm^{-2}][a]	-1 V [A cm^{-2}][b]	-2 V [A cm^{-2}][c]
C_{60}	9.57×10^{-9}	5.83×10^{-8}	4.01×10^{-7}
CN-T2T	5.45×10^{-9}	2.06×10^{-8}	9.32×10^{-8}
C_{60}:CN-T2T	5.86×10^{-9}	3.83×10^{-8}	1.96×10^{-7}

Dark current density at [a] -0.5 V, [b] -1 V, and [c] -2 V; The data are extracted from **Figure 4.1**.
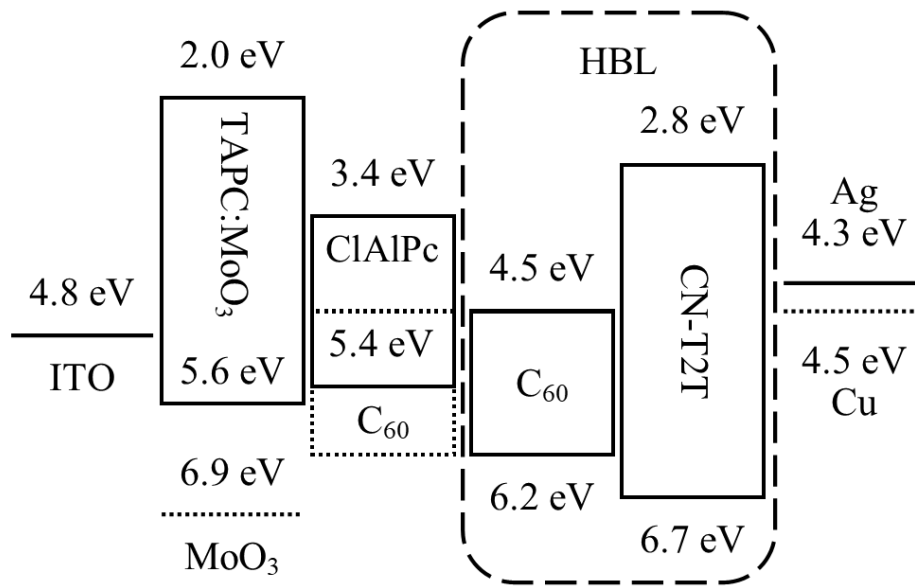
Figure 4.2 Device structure's energy level.

EQE and responsivity spectra have two peaks at 350 nm and 730 nm as can be seen in **Figure 4.3**, the first peak (UV peak) corresponds to the absorption of C_{60}, while the second peak (NIR peak) is due to the absorption of ClAlPc. EQE and responsivity of TPD with HBL of CN-T2T are the

highest among C_{60} or C_{60}:CN-T2T. The value of each peak for different HBL is listed in **Table 4.2**.

(a) EQE spectra, **(b)** responsivity spectra
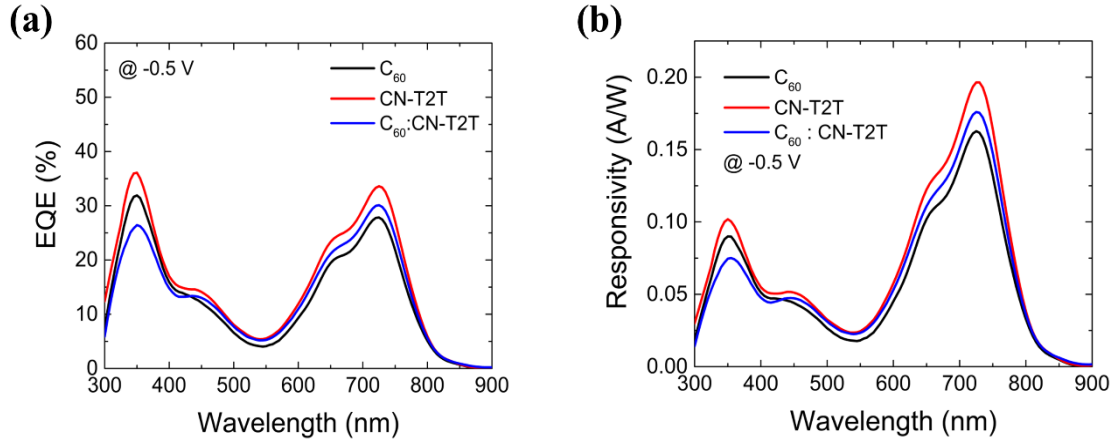
Figure 4.3 (a) EQE and (b) responsivity spectra of TPDs under -0.5 V applied bias with with HBL of C_{60}, CN-T2T, and C_{60}:CN-T2T (1:1).

Table 4.2 EQE and responsivity peaks of TPD under -0.5 V applied bias with HBL of C_{60}, CN-T2T, and C_{60}:CN-T2T (1:1).

HBL	UV peak of EQE [%][a]	NIR peak of EQE [%][b]	UV peak of responsivity [A W^{-1}][c]	NIR peak of responsivity [A W^{-1}][d]
C_{60}	31.89	27.43	0.09	0.16
CN-T2T	36.08	33.36	0.10	0.19
C_{60}:CN-T2T	26.44	29.79	0.07	0.17

Peak of EQE at wavelength of [a] 350 nm and [b] 730 nm; Peak of responsivity at wavelength of [c] 350 nm and [d] 730 nm; The data are extracted from **Figure 4.3**.

Another parameter associates with dark current density and responsivity data is specific detectivity that can be obtained by substituting the noise current with the shot noise as mentioned in **eq. (5)** and **eq. (7),** or simply by **eq. (8)**. **Figure 4.4** and **Table 4.3** show specific detectivity value at 730 nm under -0.5 V applied bias is 2.92×10^{12}, 4.69×10^{12}, and 4.04×10^{12} Jones for C_{60}, CN-T2T, and C_{60}:CN-T2T respectively. Specific detectivity, EQE, responsivity and dark current density data indicate that CN-T2T is the optimized HBL in this group of materials. Nevertheless, HBL of 10 nm CN-

T2T shows a dark current density of 9.32×10^{-8} A cm^{-2} under -2 V applied bias, which potentially can be further reduced by tuning the thickness of CN-T2T.
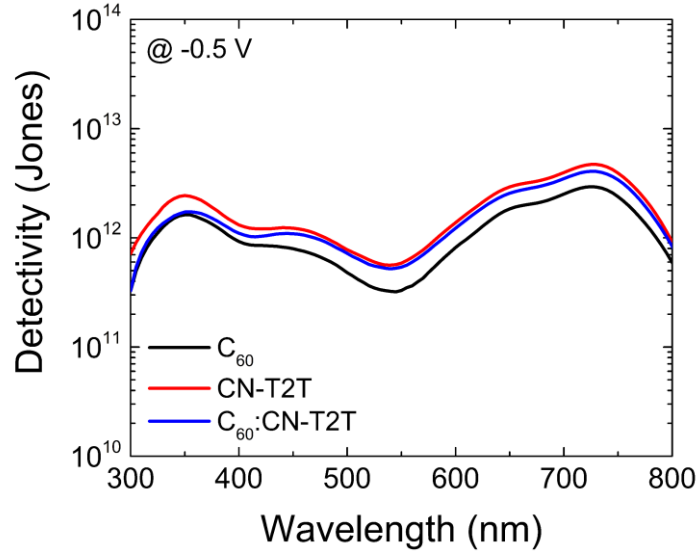
Figure 4.4 Specific detectivity of TPDs under -0.5 V applied bias with with HBL of C$_{60}$, CN-T2T, and C$_{60}$:CN-T2T (1:1).

Table 4.3 Specific detectivity peaks of TPDs under -0.5 V applied bias with HBL of C$_{60}$, CN-T2T, and C$_{60}$:CN-T2T (1:1).

HBL	UV peak of EQE [Jones][a]	NIR peak of EQE [Jones][b]
C$_{60}$	1.62×10^{12}	2.92×10^{12}
CN-T2T	2.44×10^{12}	4.69×10^{12}
C$_{60}$:CN-T2T	1.72×10^{12}	4.04×10^{12}

Peaks of specific detectivity at wavelength of [a] 350 nm and [b] 730 nm; The data are extracted from **Figure 4.4**.

4.2 CN-T2T Thickness Optimization

Device structure for HBL thickness optimization consists of ITO/TAPC:MoO$_3$ (10:1, 25 nm)/ClAlPc:C$_{60}$ (1:2, 40 nm)/HBL (x nm)/Cu:Ag (1:50, 8 nm)/WO$_3$ (30 nm). HBL in this structure is CN-T2T with different thickness of 10, 20, 30, and 40 nm. As shown in **Figure 4.5**,
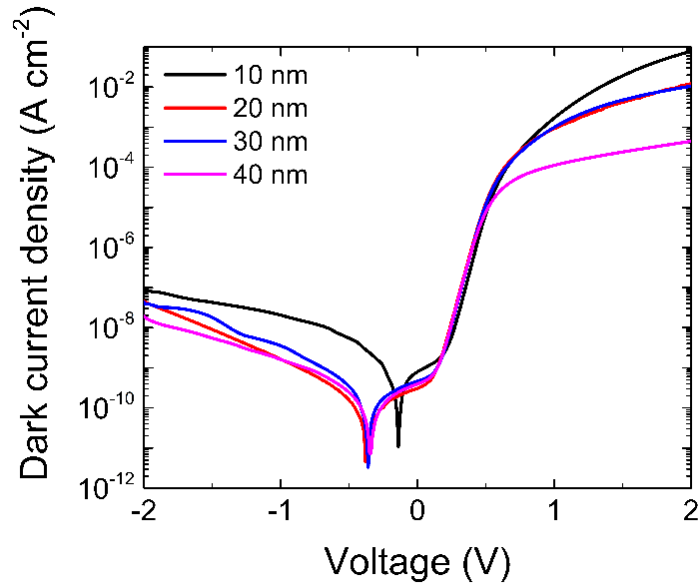
Figure 4.5 Dark current density of TPDs with with CN-T2T thickness of 10, 20, 30, and 40 nm.

Table 4.4 Summary of dark current density at different point of voltage with CN-T2T thickness of 10, 20, 30, and 40 nm.

CN-T2T	Dark current density		
	-0.5 V [A cm^{-2}][a]	-1 V [A cm^{-2}][b]	-2 V [A cm^{-2}][c]
10 nm	5.46×10^{-9}	2.06×10^{-8}	9.32×10^{-8}
20 nm	1.56×10^{-10}	1.64×10^{-9}	4.62×10^{-8}
30 nm	3.45×10^{-10}	3.53×10^{-9}	4.29×10^{-8}
40 nm	2.42×10^{-10}	1.61×10^{-9}	1.91×10^{-8}

Dark current density at [a] -0.5 V, [b] -1 V, and [c] -2 V; The data are extracted from **Figure 4.5**.

dark current density under -2 V applied bias is 9.32×10^{-8}, 4.62×10^{-8}, 4.29×10^{-8}, and 1.91×10^{-8} A cm^{-2} for CN-T2T thickness 10, 20, 30, and 40 nm respectively. Dark current density decreases as thickness of CN-T2T increases. Regarding the reciprocal relation between specific detectivity and dark current density, thicker CN-T2T monotonically increases the TPD performance, however, other parameters such as EQE and responsivity may decrease more significantly due to thicker CN-T2T that resulting a lower

overall TPD performances. The values of dark current density in **Figure 4.5** under applied bias of -0.5, -1, and -2 V are shown in **Table 4.4**.
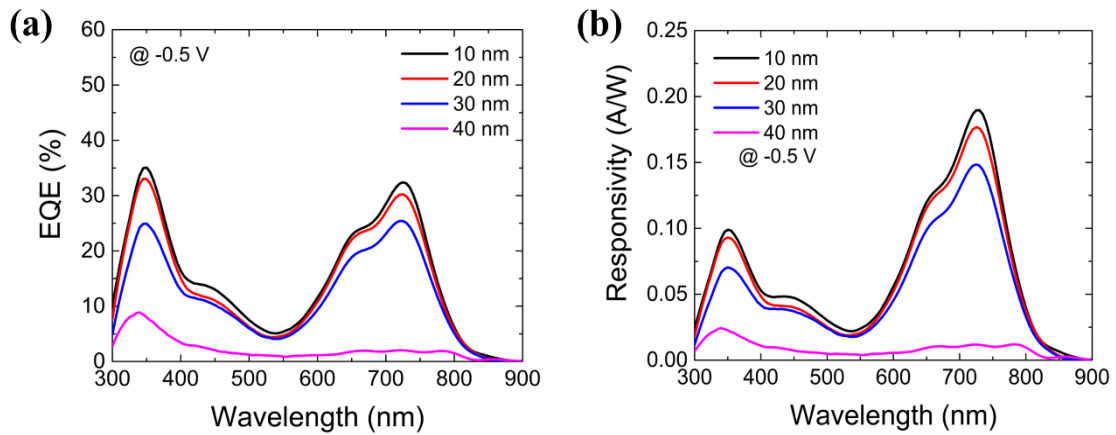
Figure 4.6 EQE and responsivity spectra under -0.5 V applied bias with different thickness of CN-T2T.

Table 4.5 EQE and responsivity peaks of TPD under -0.5 V applied bias with different thickness of CN-T2T.

CN-T2T	UV peak of EQE [%][a]	NIR peak of EQE [%][b]	UV peak of responsivity [A W^{-1}][c]	NIR peak of responsivity [A W^{-1}][d]
10 nm	35.07	32.19	0.10	0.19
20 nm	32.98	29.87	0.09	0.18
30 nm	24.93	25.06	0.07	0.15
40 nm	8.00	1.97	0.02	0.01

Peak of EQE at wavelength of [a] 350 nm and [b] 730 nm; Peak of responsivity at wavelength of [c] 350 nm and [d] 730 nm; The data are extracted from **Figure 4.6**.

As shown in **Figure 4.6** and **Table 4.5**, EQE and responsivity spectra are higher with CN-T2T thickness of 10 nm then the spectra decrease as the thickness increase, furthermore, the spectra values are extremely low with 40 nm of CN-T2T. Responsivity and dark current density exhibit opposite characteristics as the thickness of CN-T2T increase. Responsivity tend to decrease as the thickness increase which reduce the TPD performance,

oppositely, dark current density tend to decrease as the thickness increase that enhance the TPD performance. To observe the accumulative outcome of those opposite effects, specific detectivity can more accurately determine the dependency of CN-T2T thickness to the TPD performance.
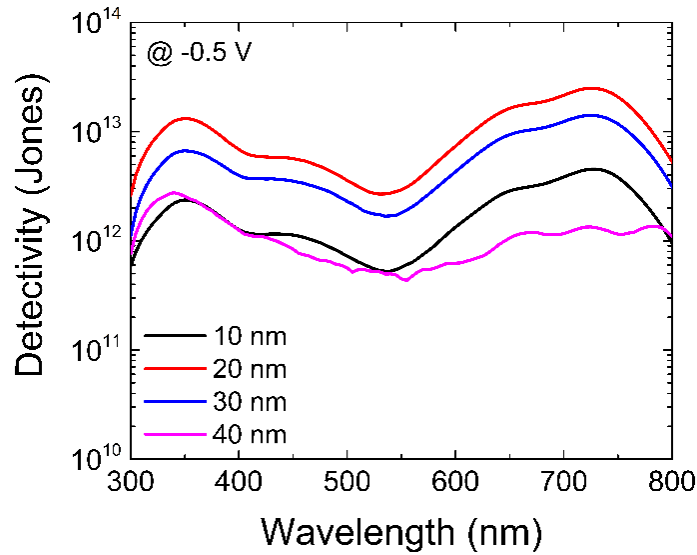
Figure 4.7 Specific detectivity under -0.5 V applied bias with CN-T2T thickness of 10, 20, 30, and 40 nm.

Table 4.6 Detectivity peaks of TPD under -0.5 V applied bias with with different thickness of CN-T2T.

CN-T2T	UV peak of EQE [Jones][a]	NIR peak of EQE [Jones][b]
10 nm	2.37×10^{12}	4.53×10^{12}
20 nm	1.32×10^{12}	2.48×10^{13}
30 nm	6.69×10^{12}	1.40×10^{12}
40 nm	2.56×10^{12}	1.32×10^{12}

Peak of specific detectivity at wavelength of [a] 350 nm and [b] 730 nm; The data are extracted from **Figure 4.7**.

As provided in **Figure 4.7** and **Table 4.6**, specific detectivity at 730 nm under -0.5 V applied bias is 4.53×10^{12}, 2.48×10^{13}, 1.4×10^{13}, and 1.32×10^{12} Jones for thickness 10, 20, 30, 40 nm respectively, which indicate that

the optimized thickness of CN-T2T is 20 nm. Therefore, 20 nm of CN-T2T is the most balanced trade-off between hole blocking capability to reduce dark current density and electron extraction capability to extract photo-generated carrier. This result is possibly due to the transit time imbalance electron and hole when the thickness of CN-T2T increase which is resulting a lower EQE and responsivity spectra [36,37].

In order to comprehensively examine the performance of TPDs with different thickness of CN-T2T, photocurrent density is measured under one sun illumination, as shown in **Figure 4.8** photocurrent density decrease as the thickness of CN-T2T increase which can be attributed to the transit time imbalance [36,37]. From **Figure 4.8** and **Table 4.4**, current-gain that is defined as J_{photo}/J_{dark} can be evaluated. The current-gain value under -0.5 V applied bias is 8.17×10^5, 2.88×10^7, 9.01×10^6, and 5.93×10^6 for thickness 10, 20, 30, and 40 nm respectively. Moreover, the transmittance spectra of TPDs with different thickness of CN-T2T depict in **Figure 4.9**, the AVT value is 72.69, 71.89, 71.42, and 71.50% for CN-T2T of 10, 20, 30, and 40 nm respectively.

Figure 4.8 Photocurrent density of TPDs under one sun illumination with CN-T2T thickness of 10, 20, 30, and 40 nm.

Figure 4.9 Transmittance spectra and AVT of TPDs with CN-T2T thickness of 10, 20, 30, and 40 nm.
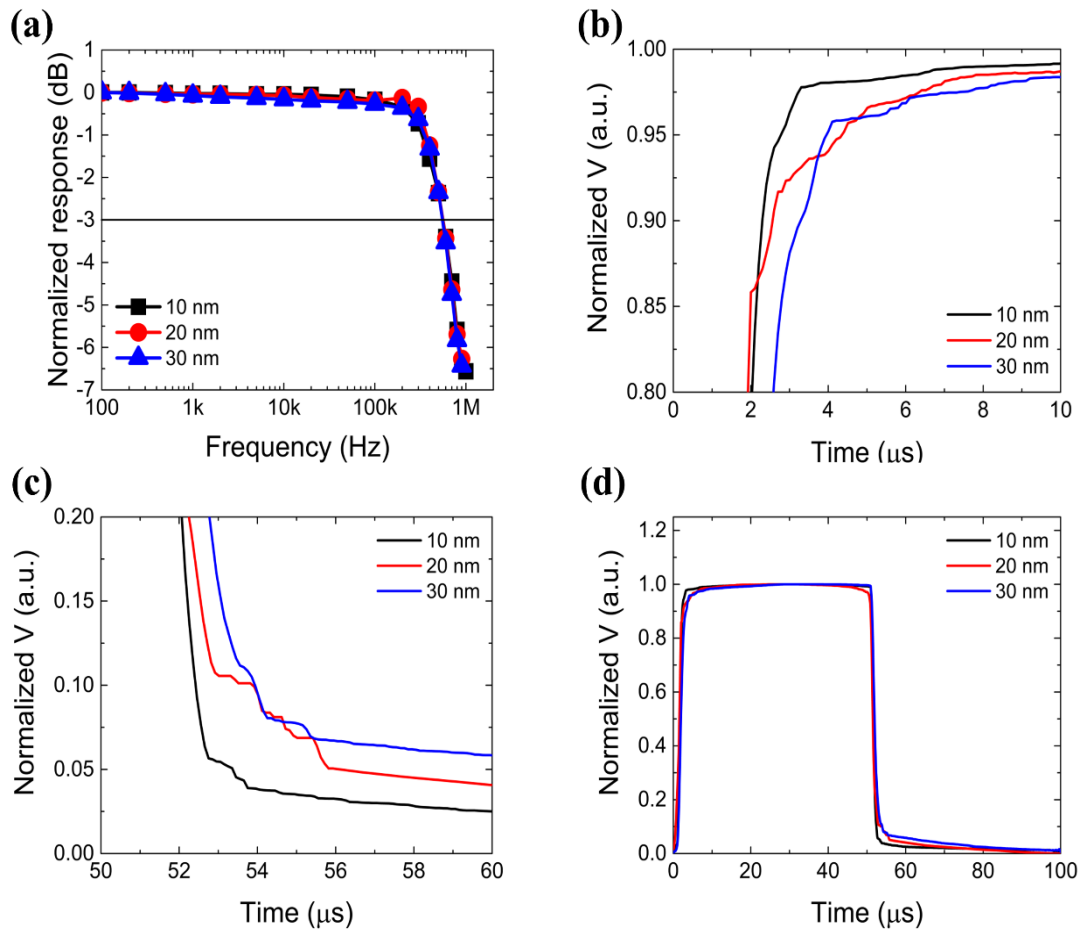
Figure 4.10 (a) $f_{-3\ dB}$, (b) rise time, (c) fall time, and (d) photoresponse for TPDs with CN-T2T thickness of 10, 20, and 30 nm under -0.5 V.

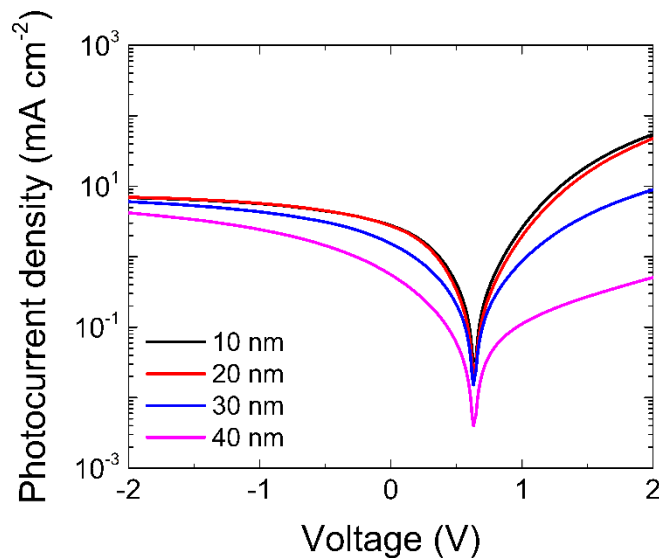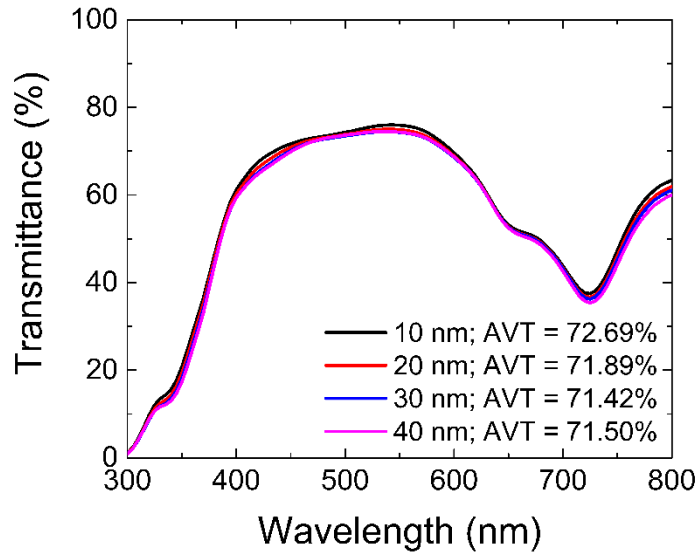**Table 4.7** Sumarry of rise time, fall time, and $f_{-3\,dB}$ cut-off under -0.5 V for CN-T2T thickness of 10, 20, and 30 nm.

CN-T2T	Rise time [μs][a]	Fall time [μs][b]	-3dB [kHz][c]
10 nm	1.06	1.20	558
20 nm	1.86	1.91	557
30 nm	2.70	2.51	552

[a] Rise time data are extracted from **Figure 4.10 (b)**, [b] Fall time data are extracted from **Figure 4.10 (c)**, and [c] $f_{-3\,dB}$ cut-off data are extracted from **Figure 4.10 (a)**.

The $f_{-3\,dB}$ measurement is taken as can be seen in **Figure 4.10**. Due to the low value of EQE of 40 nm of CN-T2T, photoresponse of the TPD is very poor and can be discarded without loss of generality in the discussion, while for CN-T2T thickness of 10, 20, and 30 nm show insignificant difference in $f_{-3\,dB}$ response, with $f_{-3\,dB}$ cut-off value of 558, 557, and 552 kHz for thickness 10, 20, and 30 nm respectively. On the other hand, the dependency of CN-T2T thickness in rise time and fall time are more obvious than $f_{-3\,dB}$ responses, namely the rise time and fall time increase as the thickness of CN-T2T increase. As previously mentioned, the increment of rise/fall time is due to the transit time imbalance [36,37]. The values of rise time, fall time, and $f_{-3\,dB}$ cut-off are shown in **Table 4.7**.

LDR, as shown in **Figure 4.11** for different thickness of 10, 20, and 30 nm is shows insignificant difference with the value of 106.71, 105.83, and 102.50 dB respectively. The LDR value for 40 nm CN-T2T thickness is omitted due to the low light response behavior. Regarding the data of specific detectivity, photo-response, and LDR, 20 nm CN-T2T is the optimized thickness for HBL which has the highest detectivity and lowest dark current density as well as maintains EQE, responsivity, $f_{-3\,dB}$, rise/fall time, and LDR nearly equivalent to the highest value of each metric. TPDs with 20 nm CN-

T2T are further examined with thermal shock of 100 °C for 1, 2, 3, and 4 hours.
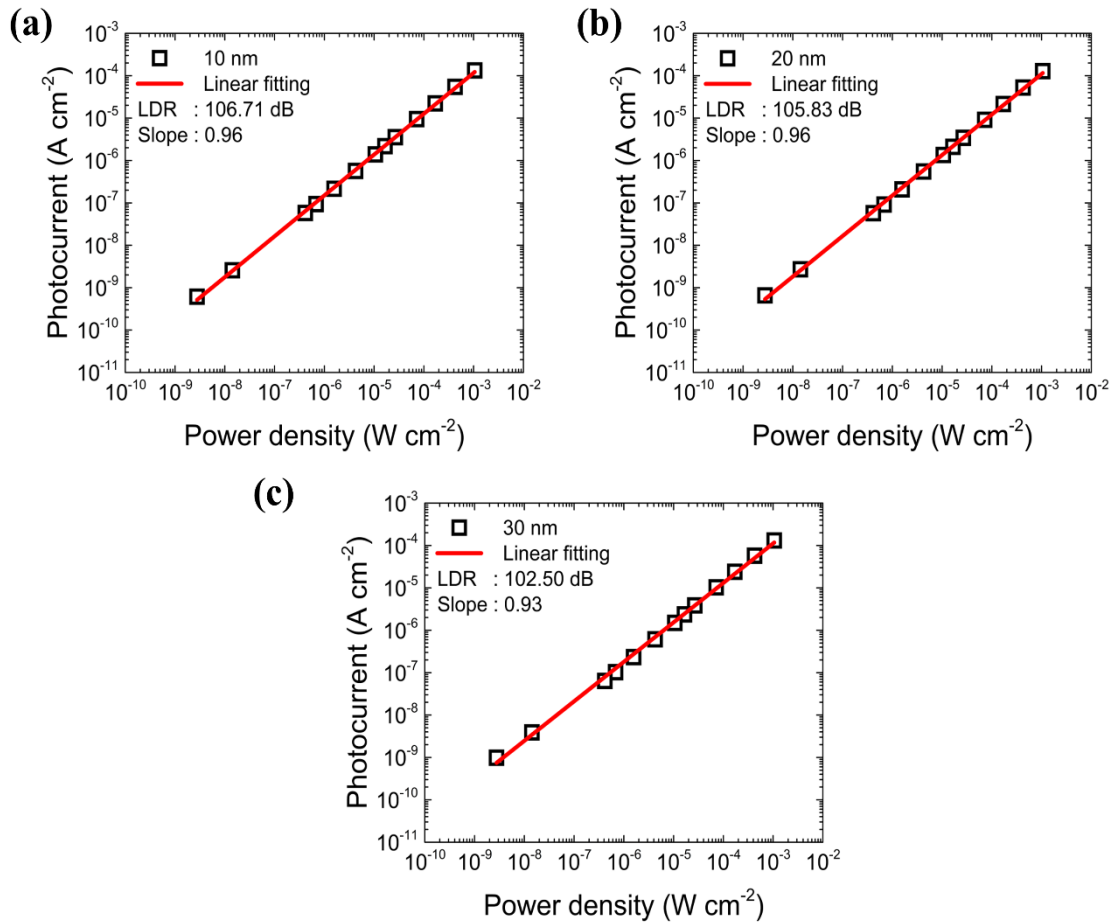
Figure 4.11 LDR of TPDs under -0.5 V applied bias with CN-T2T thickness of (a) 10 nm, (b) 20 nm, and (c) 30 nm.

4.3 Thermal Shock and Voltage Adjustment

Dark current density of TPD with 20 nm of CN-T2T after 1, 2, 3, and 4 hours are shown in **Figure 4.12**. It is shown that dark current density remains stable after 1 hour of 100 °C thermal shock, then dark current density in reverse bias rises approximately one order of magnitude after 2 hours of thermal shock and slightly increases after 3 hours and 4 hours of thermal shock. The values of dark current density under -0.5 V, -1 V, and -2 V after thermal shock are shown in **Table 4.8**.
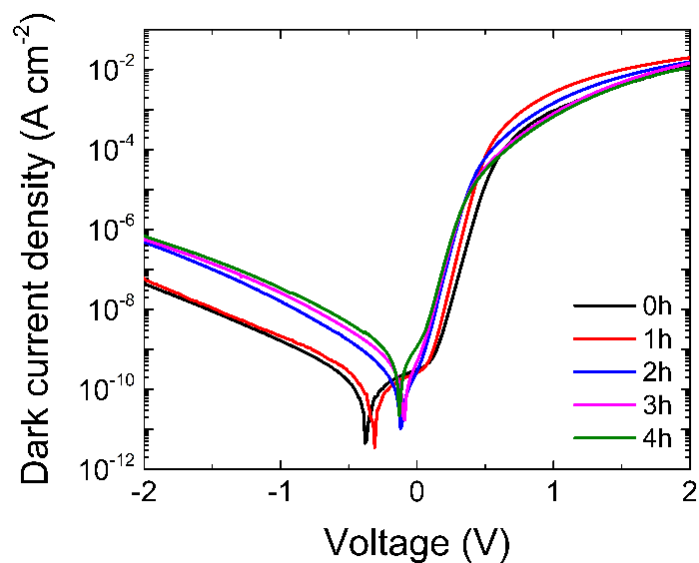
Figure 4.12 Dark current density of TPD with 20 nm CN-T2T after 100 ℃ thermal shock of 1, 2, 3, and 4 hours.

Table 4.8 Summary of dark current density in different point of voltage after 100 ℃ thermal shock of 1, 2, 3, and 4 hours.

Thermal shock	Dark current density		
	-0.5 V [A cm^{-2}][a]	-1 V [A cm^{-2}][b]	-2 V [A cm^{-2}][c]
0 h	1.56×10^{-10}	1.64×10^{-9}	4.62×10^{-8}
1 h	2.72×10^{-10}	2.13×10^{-9}	5.99×10^{-8}
2 h	1.67×10^{-9}	1.59×10^{-8}	4.93×10^{-7}
3 h	3.08×10^{-9}	2.59×10^{-8}	5.70×10^{-7}
4 h	4.60×10^{-9}	3.39×10^{-8}	6.93×10^{-7}

Dark current density at [a] -0.5 V, [b] -1 V, and [c] -2 V; The data are extracted from **Figure 4.12**.
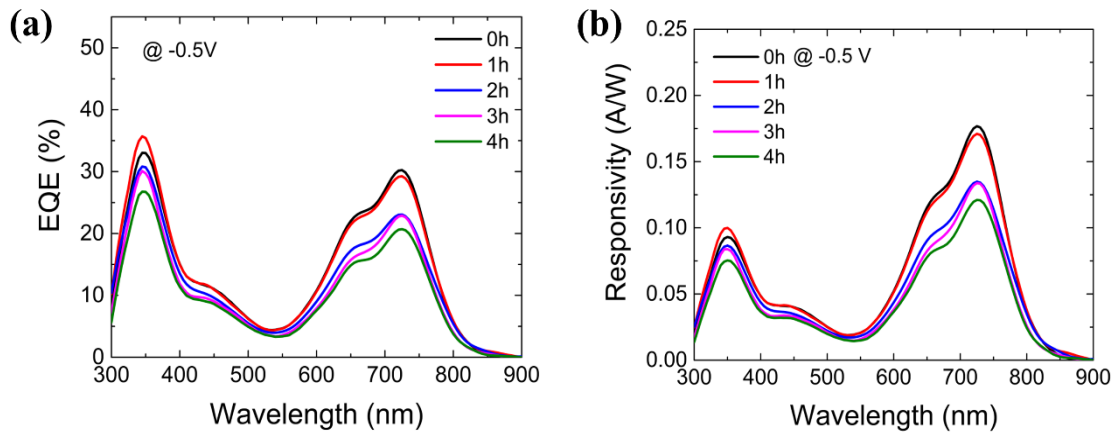
Figure 4.13 EQE and responsivity of TPD under -0.5 V applied bias with 20 nm of CN-T2T after thermal shock of 1, 2, 3, and 4 hours.

Table 4.9 EQE and responsivity peaks of TPD under -0.5 V applied bias after 100 °C thermal shock of 1, 2, 3, and 4 hours.

Thermal shock	UV peak of EQE [%][a]	NIR peak of EQE [%][b]	UV peak of responsivity [A W^{-1}][c]	NIR peak of responsivity [A W^{-1}][d]
0 h	32.98	29.86	0.093	0.18
1 h	35.42	28.91	0.099	0.17
2 h	30.68	22.79	0.086	0.13
3 h	29.73	22.64	0.084	0.13
4 h	26.71	20.52	0.075	0.12

Peak of EQE at wavelength of [a] 350 nm and [b] 730 nm; Peak of responsivity at wavelength of [c] 350 nm and [d] 730 nm; The data are extracted from **Figure 4.13**.

The similar pattern also emerges in EQE and responsivity spectra after thermal shock as shown in **Figure 4.13** and **Table 4.9**. Particularly in NIR region, EQE and responsivity are unaltered after 1 hour of 100 °C thermal shock, then decrease after 2 hours of thermal shock, it continues to slightly decrease after thermal shock of 3 hours and 4 hours.
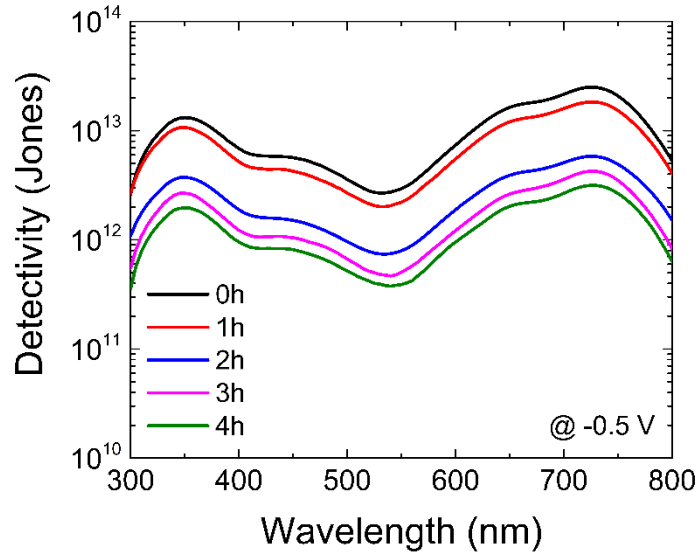
Figure 4.14 Specific detectivity of TPD under -0.5 V applied bias after thermal shock of 1, 2, 3, and 4 hours.

Table 4.10 Detectivity peaks of TPD under -0.5 V applied bias after 100 ℃ thermal shock of 1, 2, 3, and 4 hours.

Thermal shock	UV peak of detectivity [Jones][c]	NIR peak of detectivity [Jones][d]
0 h	1.32×10^{13}	2.48×10^{13}
1 h	1.07×10^{13}	1.82×10^{13}
2 h	3.74×10^{12}	5.80×10^{12}
3 h	2.67×10^{12}	4.24×10^{12}
4 h	1.96×10^{12}	3.15×10^{12}

Peak of specific detectivity at wavelength of [a] 350 nm and [b] 730 nm; The data are extracted from **Figure 4.14**.

Specific detectivity under -0.5 V applied bias is shown in **Figure 4.14**, The value of specific detectivity only slightly decrease after 1 hour of thermal shock, then decrease roughly one order of magnitude after 2 hours of thermal shock, and it continues to decrease after 3 and 4 hours of thermal shock. The peaks of specific detectivity in UV and NIR region after thermal shock are shown in **Table 4.10**. Excellent thermal stability of CN-T2T-based

TPD is due to CN-T2T has high decomposition temperature (T_d) of 418 °C and high melting temperature of 286 °C, while no evident of glass transition temperature by differential scanning calorimetry (DSC) analysis [38].
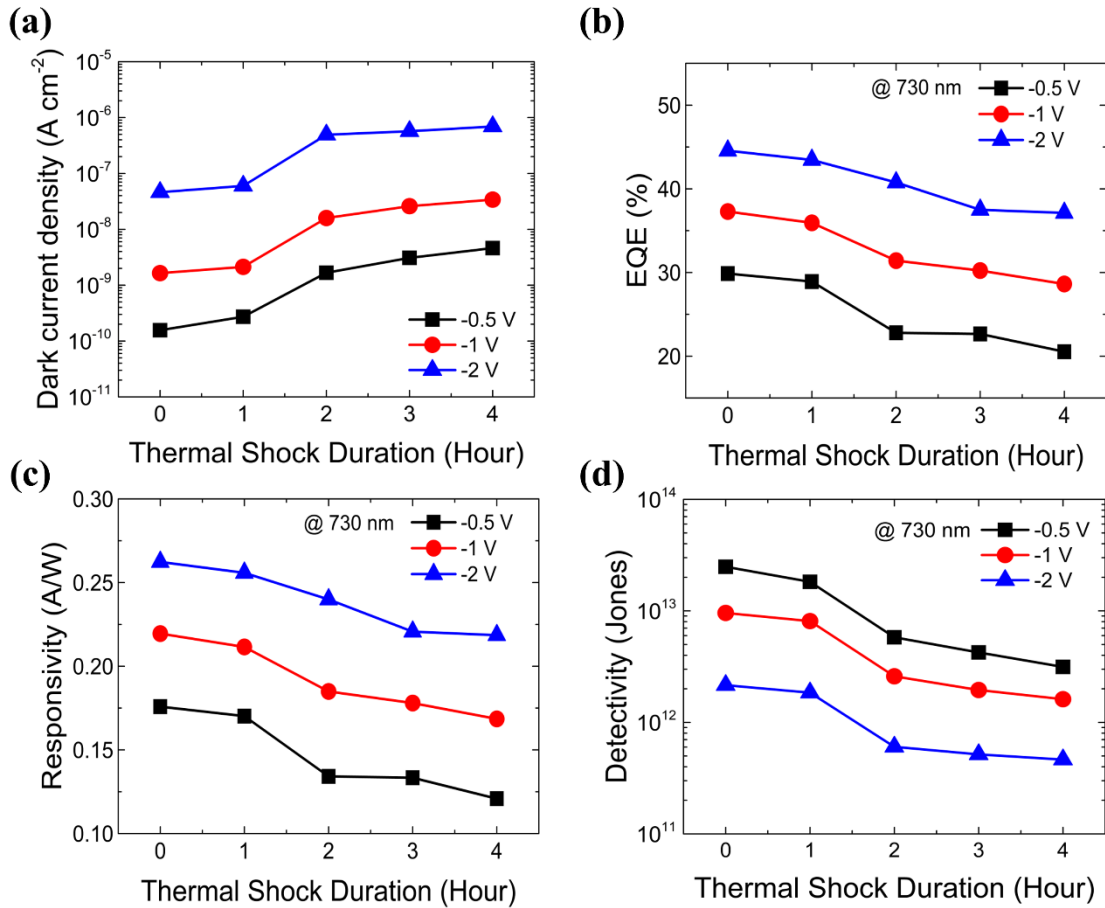
Figure 4.15 Summary of dark current density, EQE, responsivity, and specific detectivity after thermal shock with different applied bias of -0.5, -1, and -2 V.

As shown in **Figure 4.15**, the performance of dark current density is enhanced with the lower applied bias, on the contrary, EQE and responsivity are improved with the higher applied bias. However, the specific detectivity is shown higher with lower applied voltage, which indicate -0.5 V as the optimum working voltage to yield a high detectivity. This can be attributed to the lowest dark current density point in **Figure 4.12**, a higher detectivity can be achieved by choosing the applied bias nearer to the voltage in which the lowest dark current density is established (approximately at ≈-0.5 V).

5 Conclusion

There are three studies in this report, first, selection of HBL among CN-T2T, C_{60}, and CN-T2T:C_{60} (1:1), second, optimization the thickness of CN-T2T as HBL, third, thermal shock examination and working voltage adjustment to further enhance specific detectivity.

CN-T2T is the best HBL among the group materials of CN-T2T, C_{60}, and CN-T2T:C_{60} (1:1). It has been shown that TPD with CN-T2T as HBL exhibits dark current density in the order of 9.32×10^{-8} A cm^{-2}, while the other HBLs are in the order of 10^{-7} A cm^{-2}. This lower dark current density can be attributed to the lower HOMO level of CN-T2T in comparison with C_{60} which lead to a more efficient hole blocking layer than C_{60}.

Dark current density can be further reduced by tuning the thickness of CN-T2T as HBL. Thickness of 10, 20, 30, and 40 nm have been studied with 20 nm is revealed as the optimized thickness for CN-T2T. TPD with 20 nm CN-T2T show the most balanced in every aspect of performances, including the highest specific detectivity of 2.48×10^{13} Jones and the lowest dark current density of 1.56×10^{-10} A cm^{-2} while maintain EQE of 29.86%, responsivity of 0.18 A W^{-1}, AVT of 71.89%, LDR of 105.83 dB, $f_{-3\ dB}$ of 557 kHz, and rise/fall time of 1.86/1.91 μs which are nearly equivalent to the highest value of each parameter. Furthermore, TPD with a thicker CN-T2T, notably 40 nm of CN-T2T yield a poor light response owing to the transit time imbalance between electron and hole.

The optimized TPD shows excellent thermal stability under thermal shock of 100 ℃ up to one hour of exposure, no significant reduction in performances after this interval of thermal examination with the remaining dark current density of 2.72×10^{-10} A cm^{-2}, EQE of 28.91%, responsivity of 0.17 A W^{-1}, and specific detectivity of 1.82×10^{13} Jones. Performances

decrease after two hours of thermal shock with the detectivity reduce by approximately one other of magnitude then continue to slightly decrease after 3 hours and 4 hours thermal shock. Moreover, different working voltage of -0.5, -1, and -2 V have been studied to determine the optimum working voltage for these TPDs. -0.5 V is shown as the optimized working voltage due to a lower dark current density in comparison with other working voltages, this can be attributed to the lowest point of dark current density which is occurred approximately at ≈-0.5 V.

References

[1]   S.R. Forrest, Organic Electronics: Foundations to Applications, Oxford University Press, 2020. https://doi.org/10.1093/oso/9780198529729.001.0001.

[2]   I. Burgués-Ceballos, L. Lucera, P. Tiwana, K. Ocytko, L.W. Tan, S. Kowalski, J. Snow, A. Pron, H. Bürckstümmer, N. Blouin, G. Morse, Transparent organic photovoltaics: A strategic niche to advance commercialization, Joule. 5 (2021) 2261–2272. https://doi.org/10.1016/j.joule.2021.07.004.

[3]   C.J. Traverse, R. Pandey, M.C. Barr, R.R. Lunt, Emergence of highly transparent photovoltaics for distributed applications, Nat. Energy. 2 (2017) 849–860. https://doi.org/10.1038/s41560-017-0016-9.

[4]   M.Z. Li, C.C. Lee, S. Biring, I.S. Hsu, D. Luo, R. Estrada, Y.S. Wu, C.C. Yang, S.W. Liu, Vacuum-Deposited Transparent Organic Photovoltaics for Efficiently Harvesting Selective Ultraviolet and Near-Infrared Solar Energy, Sol. RRL. 5 (2021) 2000564. https://doi.org/10.1002/solr.202000564.

[5]   R.R. Lunt, V. Bulovic, Transparent, near-infrared organic photovoltaic solar cells for window and energy-scavenging applications, Appl. Phys. Lett. 98 (2011) 113305. https://doi.org/10.1063/1.3567516.

[6]   C.C. Chen, L. Dou, R. Zhu, C.H. Chung, T. Bin Song, Y.B. Zheng, S. Hawks, G. Li, P.S. Weiss, Y. Yang, Visibly transparent polymer solar cells produced by solution processing, ACS Nano. 6 (2012) 7185–7190. https://doi.org/10.1021/nn3029327.

[7]   W. Wang, C. Yan, T.K. Lau, J. Wang, K. Liu, Y. Fan, X. Lu, X. Zhan, Fused Hexacyclic Nonfullerene Acceptor with Strong Near-Infrared Absorption for Semitransparent Organic Solar Cells with 9.77%

Efficiency, Adv. Mater. 29 (2017) 1701308. https://doi.org/10.1002/adma.201701308.

[8] R.R. Lunt, Theoretical limits for visibly transparent photovoltaics, Appl. Phys. Lett. 101 (2012) 043902. https://doi.org/10.1063/1.4738896.

[9] S. Keach, TECH IT TOO FAR Samsung rival LG invents bizarre 'see-through' phone that folds completely in half, Sun. (2019). https://www.thesun.co.uk/tech/8840281/lg-foldable-phone-transparent-see-through/ (accessed December 7, 2021).

[10] C. Shin, E. Lee, B. Lee, S. Eim, Mobile Terminal, US 10254863, 2019. https://patents.google.com/patent/US10254863B2/en.

[11] S. Abbas, J. Kim, All-metal oxide transparent photodetector for broad responses, Sensors Actuators, A Phys. 303 (2020) 111835. https://doi.org/10.1016/j.sna.2020.111835.

[12] H. Zhang, S. Jenatsch, J. De Jonghe, F. Nuësch, R. Steim, A.C. Véron, R. Hany, Transparent organic photodetector using a near-infrared absorbing cyanine dye, Sci. Rep. 5 (2015) 1–6. https://doi.org/10.1038/srep09439.

[13] N. Liu, H. Tian, G. Schwartz, J.B.H. Tok, T.L. Ren, Z. Bao, Large-area, transparent, and flexible infrared photodetector fabricated using P-N junctions formed by N-doping chemical vapor deposition grown graphene, Nano Lett. 14 (2014) 3702–3708. https://doi.org/10.1021/nl500443j.

[14] Q. Li, J. van de Groep, Y. Wang, P.G. Kik, M.L. Brongersma, Transparent multispectral photodetectors mimicking the human visual system, Nat. Commun. 10 (2019) 1–8. https://doi.org/10.1038/s41467-019-12899-8.

[15] Z. Long, X. Xu, W. Yang, M. Hu, D. V. Shtansky, D. Golberg, X. Fang, Cross-Bar SnO2-NiO Nanofiber-Array-Based Transparent

Photodetectors with High Detectivity, Adv. Electron. Mater. 6 (2020) 1–8. https://doi.org/10.1002/aelm.201901048.

[16] Y.S. Lau, Z. Lan, L. Cai, F. Zhu, High-performance solution-processed large-area transparent self-powered organic near-infrared photodetectors, Mater. Today Energy. 21 (2021) 100708. https://doi.org/10.1016/j.mtener.2021.100708.

[17] M.Y. Hadiyanto, R. Estrada, C.C. Lee, S. Biring, A.K. Akbar, C.Y. Li, C.J. Shih, Y.Z. Li, S.W. Liu, Transparent photodetectors with ultra-low dark current and high photoresponse for near-infrared detection, Org. Electron. 99 (2021) 106356. https://doi.org/10.1016/j.orgel.2021.106356.

[18] Zerynth, Industrial IOT Technical Reference, (2021) 1–6. https://www.zerynth.com/download/20261/.

[19] T. Mizuno, K. Tsuno, E. Okumura, M. Nakayama, Evaluation of LIDAR system in rendezvous and touchdown sequence of hayabusa mission, Trans. Jpn. Soc. Aeronaut. Space Sci. 53 (2010) 47–53. https://doi.org/10.2322/tjsass.53.47.

[20] Apple, Apple Event — October 13, United States, 2020. https://www.youtube.com/watch?v=KR0g-1hnQPA&t=1914s.

[21] H. Ren, J. De Chen, Y.Q. Li, J.X. Tang, Recent Progress in Organic Photodetectors and their Applications, Adv. Sci. 8 (2021) 1–23. https://doi.org/10.1002/advs.202002418.

[22] W. Cao, J. Li, H. Chen, J. Xue, Transparent electrodes for organic optoelectronic devices: a review, J. Photonics Energy. 4 (2014) 040990. https://doi.org/10.1117/1.jpe.4.040990.

[23] M.Z. Li, C.C. Lee, S. Biring, I.S. Hsu, D. Luo, R. Estrada, Y.S. Wu, C.C. Yang, S.W. Liu, Vacuum-Deposited Transparent Organic Photovoltaics for Efficiently Harvesting Selective Ultraviolet and Near-Infrared Solar Energy, Sol. RRL. 5 (2021) 1–11.

https://doi.org/10.1002/solr.202000564.

[24] H. Shekhar, O. Solomeshch, D. Liraz, N. Tessler, Low dark leakage current in organic planar heterojunction photodiodes, Appl. Phys. Lett. 111 (2017) 223301. https://doi.org/10.1063/1.4996826.

[25] A.H. Fallahpour, S. Kienitz, P. Lugli, Origin of Dark Current and Detailed Description of Organic Photodiode Operation under Different Illumination Intensities, IEEE Trans. Electron Devices. 64 (2017) 2649–2654. https://doi.org/10.1109/TED.2017.2696478.

[26] M. Kielar, O. Dhez, G. Pecastaings, A. Curutchet, L. Hirsch, Long-Term Stable Organic Photodetectors with Ultra Low Dark Currents for High Detectivity Applications, Sci. Rep. 6 (2016) 1–11. https://doi.org/10.1038/srep39201.

[27] G.H. Gelinck, A. Kumar, D. Moet, J.L.P.J. Van Der Steen, A.J.J.M. Van Breemen, S. Shanmugam, A. Langen, J. Gilot, P. Groen, R. Andriessen, M. Simon, W. Ruetten, A.U. Douglas, R. Raaijmakers, P.E. Malinowski, K. Myny, X-Ray Detector-on-Plastic with High Sensitivity Using Low Cost, Solution-Processed Organic Photodiodes, IEEE Trans. Electron Devices. 63 (2016) 197–204. https://doi.org/10.1109/TED.2015.2432572.

[28] X. Zhou, D. Yang, D. Ma, Extremely Low Dark Current, High Responsivity, All-Polymer Photodetectors with Spectral Response from 300 nm to 1000 nm, Adv. Opt. Mater. 3 (2015) 1570–1576. https://doi.org/10.1002/adom.201500224.

[29] S. Valouch, C. Hönes, S.W. Kettlitz, N. Christ, H. Do, M.F.G. Klein, H. Kalt, A. Colsmann, U. Lemmer, Solution processed small molecule organic interfacial layers for low dark current polymer photodiodes, Org. Electron. 13 (2012) 2727–2732. https://doi.org/10.1016/j.orgel.2012.07.044.

[30] J.B. Park, J.W. Ha, S.C. Yoon, C. Lee, I.H. Jung, D.H. Hwang, Visible-

Light-Responsive High-Detectivity Organic Photodetectors with a 1 μm Thick Active Layer, ACS Appl. Mater. Interfaces. 10 (2018) 38294–38301. https://doi.org/10.1021/acsami.8b13550.

[31] C.D. Motchenbacher, J.A. Connelly, Low-Noise Electronic System Design, John Wiley & Sons, Inc., 1993.

[32] H.W. Ott, Noise Reduction Techniques in Electronic Systems, 2nd ed., John Wiley & Sons, Inc., 1988.

[33] Z. Wu, W. Yao, A.E. London, J.D. Azoulay, T.N. Ng, Elucidating the Detectivity Limits in Shortwave Infrared Organic Photodiodes, Adv. Funct. Mater. 28 (2018) 1–9. https://doi.org/10.1002/adfm.201800391.

[34] C.C. Lee, R. Estrada, Y.Z. Li, S. Biring, N.R. Al Amin, M.Z. Li, S.W. Liu, K.T. Wong, Vacuum-Processed Small Molecule Organic Photodetectors with Low Dark Current Density and Strong Response to Near-Infrared Wavelength, Adv. Opt. Mater. 8 (2020) 1–10. https://doi.org/10.1002/adom.202000519.

[35] G. Simone, M.J. Dyson, S.C.J. Meskers, R.A.J. Janssen, G.H. Gelinck, Organic Photodetectors and their Application in Large Area and Flexible Image Sensors: The Role of Dark Current, Adv. Funct. Mater. 30 (2020) 1904205. https://doi.org/10.1002/adfm.201904205.

[36] S. Ullbrich, B. Siegmund, A. Mischok, A. Hofacker, J. Benduhn, D. Spoltore, K. Vandewal, Fast Organic Near-Infrared Photodetectors Based on Charge-Transfer Absorption, J. Phys. Chem. Lett. 8 (2017) 5621–5625. https://doi.org/10.1021/acs.jpclett.7b02571.

[37] A. Armin, A. Yazmaciyan, M. Hambsch, J. Li, P.L. Burn, P. Meredith, Electro-Optics of Conventional and Inverted Thick Junction Organic Solar Cells, ACS Photonics. 2 (2015) 1745–1754. https://doi.org/10.1021/acsphotonics.5b00441.

[38] W.Y. Hung, P.Y. Chiang, S.W. Lin, W.C. Tang, Y.T. Chen, S.H. Liu, P.T. Chou, Y.T. Hung, K.T. Wong, Balance the Carrier Mobility to

Achieve High Performance Exciplex OLED Using a Triazine-Based Acceptor, ACS Appl. Mater. Interfaces. 8 (2016) 4811–4818. https://doi.org/10.1021/acsami.5b11895.